Interplanetary Dust Bands

Ishiguro, Masateru

(Degree)
博士（理学）

(Date of Degree)
2000-03-31

(Date of Publication)
2014-11-12

(Resource Type)
doctoral thesis

(Report Number)
甲2091

(JaLCDOI)
https://doi.org/10.11501/3173030

(URL)
https://hdl.handle.net/20.500.14094/D1002091

博士論文

Interplanetary Dust Bands
（惑星間ダストバンド）

平成１２年１月７日

神戸大学大学院 自然科学研究科

石黒 正晃

Masateru Ishiguro

Contents

[1]Adapted from Ishiguro et al., *Proc. of the 29th ISAS Lunar and Planetary Symp.*, **29**, 64, (1996)
[2]Adapted from Ishiguro et al., *Proc. of the 30th ISAS Lunar and Planetary Symp.*, **30**, 142, (1997)
[3]Adapted from Ishiguro et al., *Earth, Planets and Space*, **50**, 477, (1998)
[4]Adapted from Ishiguro et al., *ApJ*, **511**, 432, (1999a)
[5]Adapted from Ishiguro et al., *PASJ*, **51**, 363, (1999b)
[6]Adapted from Ishiguro et al., *Submitted to ApJ*
[7]Adapted from James et al., *MNRAS*, **288**, 1022, (1997)
[8]Adapted from Ishiguro et al., *PASJ*, **49**, L31, (1997)

1 General Introduction

The zodiacal light is the sunlight scattered by the interplanetary dust cloud (*i.e.*zodiacal cloud). We can see it as the cone shape elongating almost along the ecliptic plane in short time after sunset or before sunrise. The brightness of zodiacal light decreases as seeing at the larger solar elongations. It is, however, getting bright around the anti-solar point. This is called the Gegenschein, which arises from the back scattering. The intensity distribution of zodiacal light is largely related to not only the optical and dynamical properties of the dust particle, but also its origin and secular perturbation by planets. In the past several years there has been increasing interest in the relations between planets and exo-zodiacal cloud for the purpose of indirect detection of other terrestrial planets (*see e.g.* Backman et al. 1998). To accomplish this, it is very important to investigate the spatial structure of the zodiacal cloud of our solar system, which is the only system to find the existence of planets.

From the previous observation in visible wavelength, it was believed that the spatial structure of zodiacal cloud is smooth. The Infrared Astronomical Satellite(IRAS) brought us the new concepts on zodiacal cloud. IRAS's data have revealed the existence of some local heterogeneities in the interplanetary dust clouds, which arise from the spatial enhancement of dust grains supplied from comets and/or asteroids. Such local enhancements in the spatial density of dust grains are known as the dust bands(Low et al.1984), the cometary dust trails(Sykes & Walker 1992) and the resonance rings(Dermott et al.1994b). It is widely accepted that the dust bands and the dust trails have the origin of asteroids and comets, respectively, and the resonance rings consist of the dust grains trapped by the dynamical resonance with the Earth. The existence of these fine structures in the zodiacal clouds has been confirmed by COBE (Cosmic Infrared Experiment) observations. These structure tells us the information of its origin and dynamical evolution of interplanetary dust particle.

Almost all of such new findings came from the measurements in the infrared wavelengths. It was thought that such faint structure like dust bands cannot be separated from the diffuse zodiacal light by using the data obtained at ground-based observations due to the strong contamination by the atmospheric scattering/emission light. However, it is important to develop the way to detect the faint structure of the zodiacal light in visible wavelengths since we can get the 'snapshot' of widespread zodiacal light at any time in any region of the sky, while the infrared data of zodiacal emission supplied from the Earth-bounded satellite are very limited due to severe limitations in available time and viewing direction of satellite of interest.

We have started the continuous observations to measure the faint zodiacal light from the ground in visible wavelengths, under the cooperation with Dr. John James(Univ.of Manchester, UK) from 1995, by using the new technical device, *i.e.* a cooled CCD camera. We have done the photometric observation at Haleakala(3055m, Hawaii) in September 1995, at Norikura(2876m, Nagano, Japan) in September 1996, at Kiso(1130m, Nagano, Kiso) in February/March 1997. From these observations, we have obtained the outline of the spatial structure of the zodiacal cloud, and these results are summarized in Chapter 2.

Big findings were obtained from our observation at Hale Pohaku(2800m, Hawaii) in November 2, 1998, as reported in Chapter 3. This was the first detection of the interplanetary dust bands from the ground in the visible wavelengths. In Chapter 4, we have examined the diversity and similarity of the visible dust bands and infrared dust bands, based on the data obtained by our ground-based observation (Ishiguro et al. 1999a, Chapter 3) and by the Infrared Astronomical Satellite (IRAS). The evidence of dynamical evolution of dust bands particle is described based on our observation data in Chapter 5. The data used in this section are obtained at the summit of Mauna Kea, Hawaii(4200m) on December 15, 1998. The observational evidence of the dust trail associated with P/Encke is also reported in Chapter 5.

The general conclusions are summarized in Chapter 6.

2 Global Structure of Zodiacal Cloud

2.1 North-South Asymmetry of the Zodiacal Light obtained at Haleakala*[1]

2.1.1 Observation

The photometric data presented here were obtained at 3000 m altitude on Haleakala (Maui, Hawaii, USA) from the 19th August to the 25th September in 1995. In this season, the morning zodiacal light is observed nearly vertical at the eastern horizon there, so the extinction by the atmosphere and the contaminant by the airglow were minimized. A 16mm fish-eye lens was used to get widespread data of zodiacal light. The field of view was 31° × 46°, and the spatial resolution was about 4.8'/pixel. A N_2-cooled CCD camera was used to make accurate measurements of the surface brightness. Exposures were made with the horizon parallel to the short side of the frame on fixed mount, so the rows of frame were almost in parallel with the ecliptic latitude (Fig.1). The filters were set to isolate the B, V, and R photometric ranges usual in astronomy. In practice it was found that the green exposures (550 nm, width about 90 nm) were most effective for photometry and the results we reported here were made from these.

2.1.2 Data reduction

In the ground observations, the observed intensity(I_{obs}) of the light of the night sky is composed of those of starlight(I_{ST}), zodiacal light(I_{ZL}) and airglow(I_{AG}).

$$I_{obs} = (I_{ST} + I_{ZL} + I_{AG}) \cdot e^{-\tau_{eff}(z)},$$

where $\tau_{eff}(z)$ denotes the optical depth of the atmosphere. After examining the effects of the fish-eye lens and the CCD camera, we removed the stars inside the frame by computer program. The reduced data involved I_{ZL} and I_{AG}. Fig.1 shows the contour map of resulting brightness obtained at $04^h22^m21^s$ - 23^m11^s on the 23rd September.

It needs an assumption to deduce I_{AG} alone from our data. In V photometric range, the green airglow line of OI line emission at 557.7nm was the chief contamination and was easily recognized from the Van Rhijn effect that the light was well stratified horizontally and fairly uniform across the frame. Then we can regard that the position of the maximum brightness and symmetry of the zodiacal light were not influenced by the airglow. However, since the intensity of airglow has still large uncertainty, the absolute brightness of the zodiacal light will not be discussed here.

2.1.3 Results and discussion

The position of the maximum brightness of the zodiacal light were slightly shifted to the south compared with the ecliptic plane (Fig.2). Furthermore, the relative intensity of the zodiacal light along the ecliptic latitude showed some excess in the south side. This evidence leads to the north-south asymmetry of the zodiacal light (Fig.3a).

[1] Adapted from Ishiguro et al. (1996)

2.1.4 Discussion

These feature can be explained by the cloud model centered on the symmetric plane of the zodiacal cloud southward to the ecliptic plane. If the plane of symmetry of the interplanetary dust coincides with the ecliptic plane, it's maximum brightness also coincides the ecliptic plane and the intensity along the ecliptic latitude becomes symmetry. The gravitational influence of planets, however, changes the symmetric plane of the dust cloud. According to Dumont and Sanchez-Martinez(1968), the interplanetary dust outside 1 AU is distributed symmetrically to the invariable plane($\Omega = 107°, i = 1.6°$), while Leinert et al.(1980) showed, in the inner solar system, that the interplanetary dust is distributed along a plane with inclination $i = 3.0 \pm 0.3°$ and ascending node at $\Omega = 87 \pm 4°$.

Fig.3 (b),(c), and (d) are the calculated results for the cloud model along the invariable plane. They show the north-south asymmetry and the shift of the maximum brightness to the south compared with the ecliptic plane. They are in qualitative agreement with our measurements.

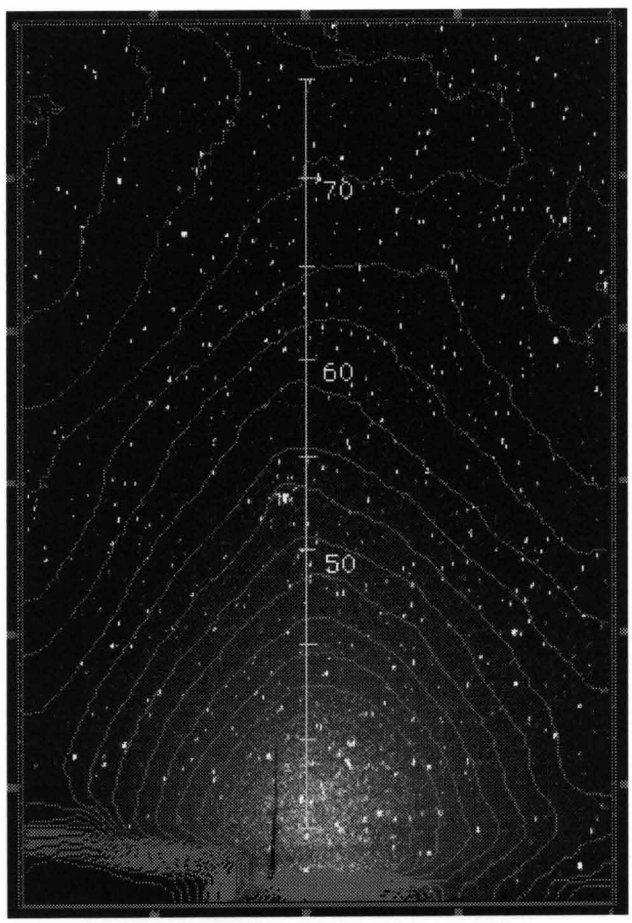

Figure 1: The zodiacal light image obtained at $04^h22^m21^s$ - 23^m11^s on the 23rd September, 1995. A nearly perpendicular line denotes an ecliptic plane with a scale of solar elongation ϵ from 35° to 75° ($285° \leq \lambda - \lambda_\odot \leq 325°$). The intensities after removing the star at the brightest and darkest parts are, respectively, 129 and 44 in arbitrary units. The contour curves were illustrated in every 5 units of this arbitrary unit.

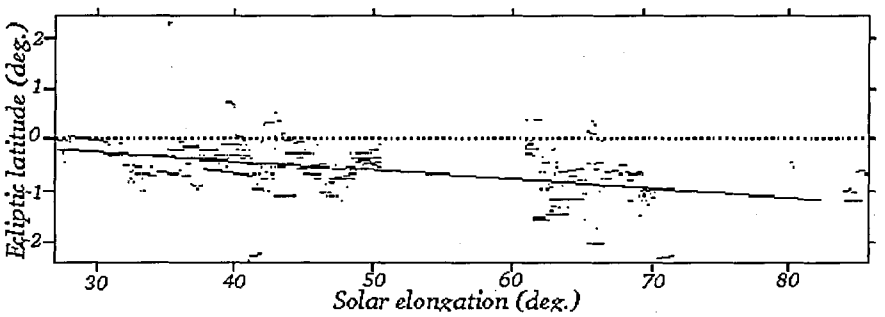

Figure 2: Maximum brightness along the elongation; $\beta < 0°$ means the south region compared with the ecliptic plane($\beta = 0°$).

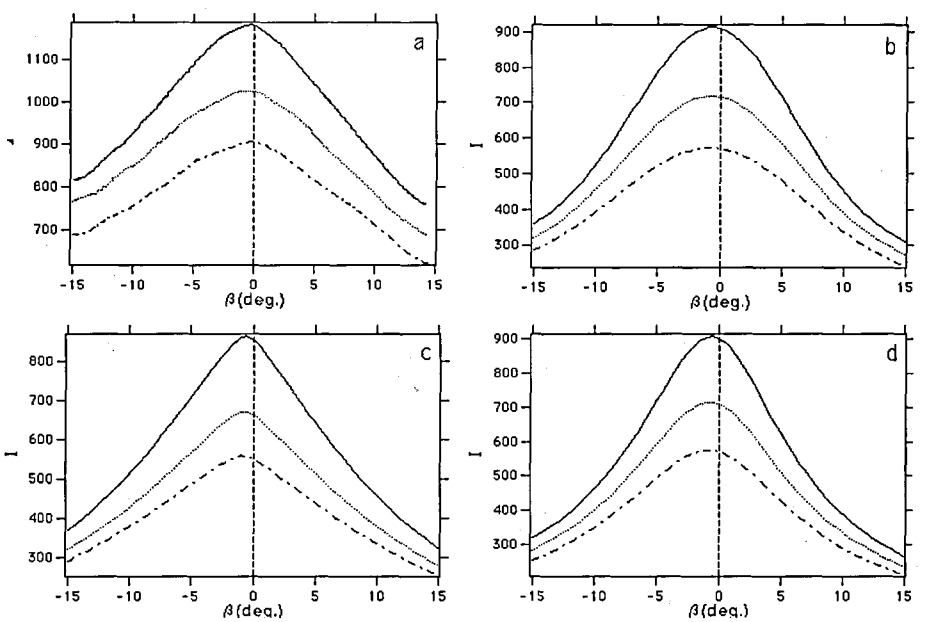

Figure 3: A comparison our measurements(a) with the calculated results (b)~(d). (b),(c), and (d) are the calculated results for cloud model along the invariable plane with different spatial distributions, namely, (b) comes from optimum sombrero model, (c) from extreme fan model and (d) from ellipsoid model. Solid line, dotted line and dashed line represent the results of calculations along a line of sight at $\epsilon = 40°, 55°, 50°$, respectively.

2.2 North-South Asymmetry of the Zodiacal Light obtained at Kiso Observatory*[2]

2.2.1 Introduction

The zodiacal light is the sunlight scattered by the interplanetary dust cloud. We can see it as the cone shape elongating almost along the ecliptic plane in short time after sunset or before sunrise(Fig.4). Roughly speaking the cone axis of the zodiacal light coincides with the symmetry plane of the zodiacal dust cloud, if it exists. The plane of symmetry of the zodiacal light observed previously is summarized in Leinert(1975). Recently, James et al.(1997) shows the north-south-asymmetry from the observation of the zodiacal light on the 22nd September in 1995. They have also reported the axis of symmetry of the zodiacal light in the morning is significantly south of the ecliptic plane. If this deviation is explained by the earth's annual motion, the feature of asymmetry changes with the season.

2.2.2 Observation

The photometric data presented here were obtained at 1130 m altitude on Kiso Observatory, Nagano, Japan between the 9th February and the 5th March in 1997. In this season, the evening zodiacal light is observed nearly vertical at the western horizon. Consequently the atmospheric extinction and the contamination by the airglow can be minimized. We used a 8mm Nikon fish-eye lens to get widespread data of zodiacal light. The pixel number of Mutoh CV-16 CCD camera is 1536 × 1024 pixels, and the pixel spacing is $9\mu m \times 9\mu m$. Since the zodiacal light is very faint object, we set up 2×2 binning. As the result, the spatial resolution becomes 7.9'/pixel and the field of view is 101° × 68°. We selected the exposure time as 20 min. The two filters of Hoya G-533 and Schott V(GG495+BG39) were applied. The former roughly corresponds to the standard V band filter. In practice the images obtained by the former filter looks to have better quality. Therefore we reported the data obtained by Hoya G-533 filter.

2.2.3 Data reduction

In the ground observations, the observed intensity(I_{obs}) of the light of the night sky is composed of those of starlight(I_{ST}), zodiacal light(I_{ZL}) and airglow(I_{AG}). In the case of our observation the contamination of the city light(I_{CL}) is not negligible in the lower sky. We suffer from the city light because the cities, such as Nagoya and Gifu, are located in about 100 km south west of Kiso observatory.

$$I_{obs} = (I_{ST} + I_{ZL} + I_{AG}) \cdot e^{-\tau_{eff(z)}} + I_{CL},$$

where $\tau_{eff(z)}$ denotes the optical depth of the atmosphere. We estimated $\tau_{eff(z)}$ from the background stars. After subtracting the dark noise, we removed the stars inside the frame by computer program. The reduced data involved I_{ZL} ,I_{AG} and I_{CL}. Fig.4 shows the image of zodiacal light obtained at 19^h20^m - 40^m on the 5th March, 1997. The dark part of lower frame is the lodgings. The straight line across the frame denotes the ecliptic plane and the numbers on it shows the values of heliocentric longitude $\lambda - \lambda_\odot$ (deg.). The contour curves are illustrated in every 150 arbitrary units.

[2]Adapted from Ishiguro et al. (1997)

It needs an assumption to deduce I_{AG} from the observed data after star removal. In V photometric range, the green airglow line of OI line emission at $557.7nm$ is the chief contamination. It is easily recognized from the Van Rhijn effect that the light was well stratified horizontally and fairly uniform across the frame. We apply the background sky brightness to appropriate exponential function and subtract it from the smoothed data. Since the intensity of airglow has still large uncertainty, the absolute brightness of the zodiacal light has not been discussed here. The residual contamination is city light. This effect is larger in the lower southward sky, that is, the low elongated from the sun ($\lambda - \lambda_\odot < 50°$). On the other hand, in $\lambda - \lambda_\odot > 65°$ the signal from the zodiacal light is too low to study significantly. As a result, we found that the useful data is in the range $\lambda - \lambda_\odot = 50°$ to $65°$.

2.2.4 Results and discussion

The position of the maximum brightness of the zodiacal light presented in this paper were slightly shifted to the north compared with the ecliptic plane (Fig.5). Furthermore, the relative intensity of the zodiacal light along the ecliptic latitude showed some excess in the north side (Fig.6). This evidence leads to the north-south asymmetry of the zodiacal light.

These feature can be explained by the cloud model centered on the symmetric plane of the zodiacal cloud northward to the ecliptic plane in February and March. If the plane of symmetry of the interplanetary dust coincides with the ecliptic plane, it's maximum brightness also coincides the ecliptic plane and the intensity along the ecliptic latitude becomes symmetry. However if the plane of symmetry is shifted from the ecliptic plane by e.g.,the gravitational influence of planets and the source distribution of the interplanetary dust, maximum brightness of the zodiacal light occurs in the region of out of the ecliptic plane. Consequently, the intensity becomes asymmetry. According to Dumont and Sanchez-Martinez(1968), the interplanetary dust outside 1 AU is distributed symmetrically to the invariable plane($\Omega = 107°, i = 1.6°$)(Fig.8), while Leinert et al.(1980) showed, in the inner solar system, that the interplanetary dust is distributed along a plane with inclination $i = 3.0 \pm 0.3°$ and ascending node at $\Omega = 87 \pm 4°$. Our results seem to support the cloud model centered on the invariable plane.

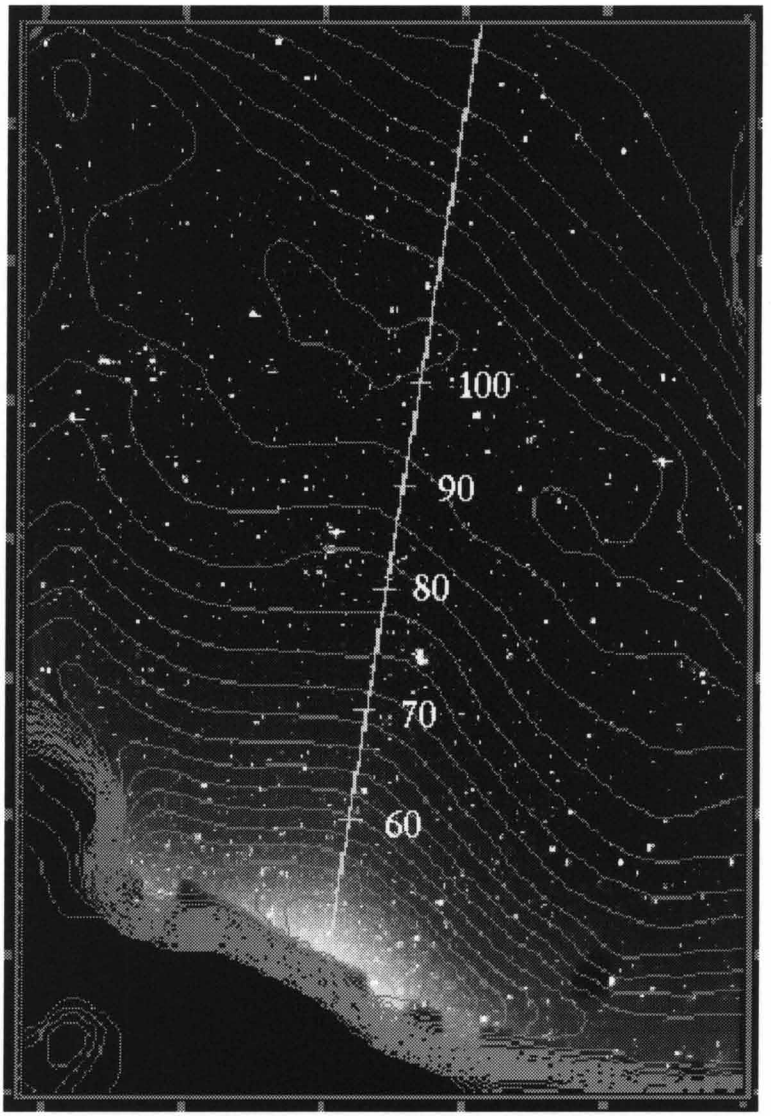

Figure 4: The image of the zodiacal light observed at Kiso Observatory on March 5, 1997 in V band filter. Straight line and numbers indicate the ecliptic plane and the heliocentric longitude, respectively

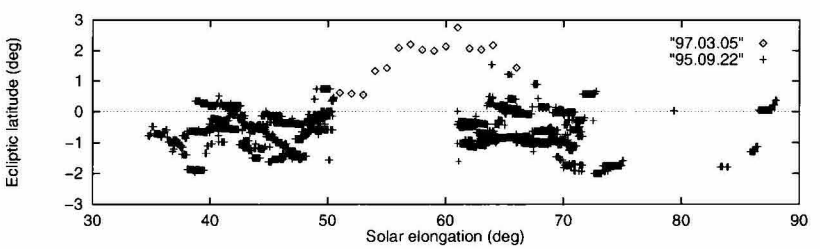

Figure 5: Maximum brightness point of each ecliptic latitude.

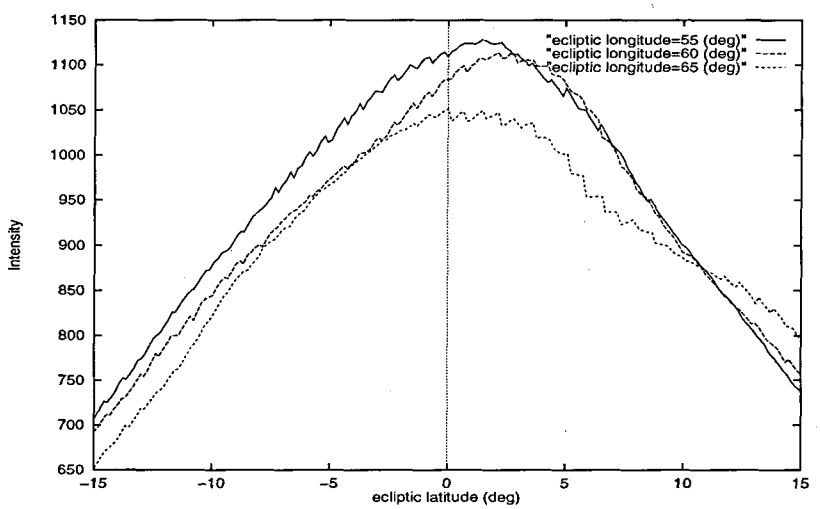

Figure 6: A comparison of our observation along the ecliptic latitude. Solid, dashed and dotted curves represent the values of $\lambda - \lambda_{\odot}$, 55°,60° and 65°, respectively.

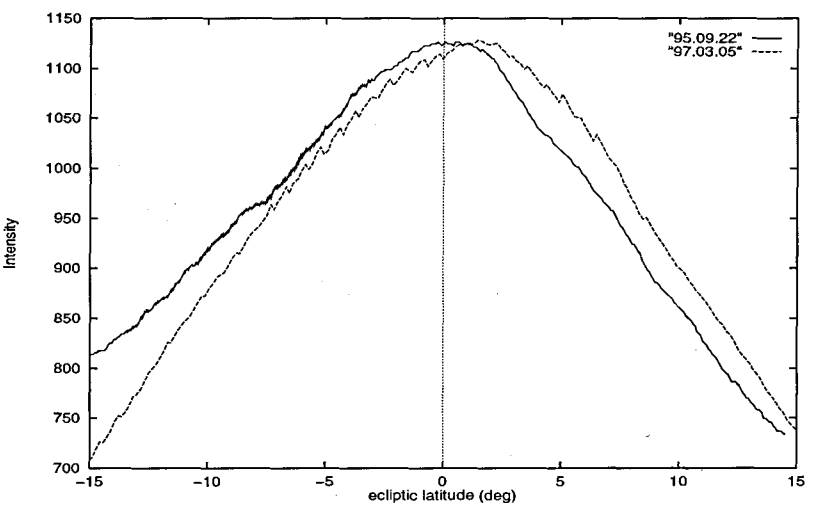

Figure 7: A comparison of the data obtained on the 21th September 1995 (Haleakala, solid curve) and the 5th March 1997 (Kiso, dashed curve).

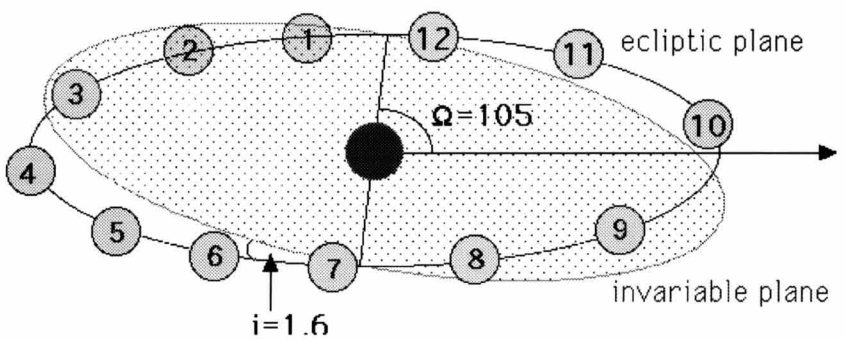

Figure 8: Geometry of the invariable plane. The numbers indicate the position of the Earth at the beginning of the respective month.

2.3 The Isophote Maps of the Gegenschein Obtained by CCD Observations*[3]

2.3.1 Introduction

The Gegenschein is an extremely faint light around the antisolar point. Such faint excess of light was explained by many hypotheses (see, *e.g.* the review by Roosen 1971), such as the reflected sunlight by particles concentrated near the libration point in the Earth-Moon system, the emission from the Earth's gaseous tail, the scattered sunlight by Earth's dust tail cloud, and the scattered sunlight by the interplanetary dust cloud. Since the Gegenschein is still present in Pioneer 10 data out to 1.86 *AU* (Weinberg *et al.* 1973), it is widely accepted that the Gegenschein is the enhancement of the scattered sunlight in the back-ward direction by the interplanetary dust grains. However there still remain some questions about the Gegenschein.

The first question is its exact position of the maximum brightness. Tanabe (1965) reported that the position of the photometric center of the Gegenschein moved periodically to both sides of the ecliptic; to the north in spring and to the south in autumn. Roosen (1970) and Leinert (1976) cited that Dumont (1965) reported the maximum brightness coincided with the antisolar point. However, as a reviewer of the manuscript, Dumont makes the comment that 'Despite their poorer definition (the netmesh of 4°), my Gegenschein isophotes (Fig. VI-4, p.306 in Dumont (1965)), observed in February, are in good agreement with the present isophotes shown in Fig.10 , because i) they exhibit a northward shift (2° or 3°) of the brightness peak along scans perpendicular to the ecliptic at longitudes ±5° to ±10° right and left of the antisun, and ii) as approaching the antisolar longitude, this shift decreases and almost vanishes, a trend which also appears in both Figs. 9 and 10 of the present work'.

The second question is the value of its excess brightness. When we observe the Gegenschein, we measure the total brightness coming from the different sources, *i.e.* the scattered light from urban lightning (the city light), the airglow emission, the scattered sunlight by lower atmosphere of the Earth, the light of background stars (integrated starlight), as well as the Gegenschein. Leinert (1975) reported the maximum brightness of the Gegenschein is about 200 $S_{10\odot}$ and its excess brightness is about 40 $S_{10\odot}$, where the equivalent of 1 $S_{10\odot}$ at a wavelength of 530 nm is $1.23\times10^{-8}Wm^{-2}sr^{-1}\mu m^{-1}$. Subtraction of other elements to get the excess brightness of the Gegenschein alone is still very difficult task.

The third question is its shape. In general the shape of the Gegenschein is oval elongating east-west direction (*e.g.* Roosen 1971). It was difficult to define its precise shape photometrically because there was no available detector for mapping the faint diffuse object, such as the Gegenschein simultaneously. However, it is getting easier recently to take an isophote map of the Gegenschein by using the cooled CCD camera attached to the fish-eye lens, as we used here.

Main purpose of our observations presented here is to measure the shape of the Gegenschein by using the cooled CCD camera, and subsequently to estimate the position of its maximum brightness, and also to monitor their variations with the season. It is rather difficult to obtain the absolute brightness of the Gegenschein, because of the inevitable dark noise in CCD. We checked the dark noise in the evening and after the dawn every day, and found that the efficiency of the refrigerator was not stable. Since a slight varia-

[3]Adapted from Ishiguro et al. (1998)

tion of the dark noise might be included in the data, we will not discuss here the absolute brightness of the Gegenschein.

2.3.2 Observations

The photometric data presented here consist of three different observations; at Norikura($2876m$, Nagano, Japan) in September, 1996 and Kiso($1130m$, Nagano, Japan) in February and March, 1997. The details of each observation are as follows.

(I)Norikura

Exposures were made in the 18th September, 1996 at the Norikura Observatory (altitude $2876m$, latitude $36°6.8'N$), which is one branch of the National Astronomical Observatory, Japan. We used the instrument consisting of the $20mm$ F5.6 wide angle lens attached to the Mutoh CV-16 CCD camera. The number of pixels of Mutoh CV-16 CCD camera is 1536×1024 *pixels*, and the pixel spacing is $9\mu m \times 9\mu m$. Since the Gegenschein is very faint object, we set up 2×2 binning. As the result, the spatial resolution becomes 3.0'/pixel and the field of view is 38°×25°. The exposure time was selected as 20 *min* by using the equatorial. The filter of Hoya G-533 was applied, which roughly corresponds to the standard V band filter. Since the sky was very fine and clear in the 18th September, 1996, we could get the significant data by one night observation alone.

The zenith angle z of the Gegenschein at midnight was 38° in Sept. 18, 1996. Since the large cities of Nagoya and Gifu are located in the direction of south-west, the contamination of the city light in the south-west sky appeared. Therefore, the data in the lower sky than $z \geq 45°$ were discarded. As a result, the available data cover the region of sky, $167° \leq \lambda - \lambda_\odot \leq 193°, -7° \leq \beta \leq 7°$, where $\lambda - \lambda_\odot$ denotes the differential helioecliptic longitude and β means the ecliptic latitude.

(II)Kiso

At Kiso Observatory (altitude $1130m$, latitude $35°47.6'N$), we observed from the 9th to the 14th February, 1997 and in the 4th and the 5th March, 1997. We used a $8mm$ Nikon fish-eye lens to get widespread image of the Gegenschein. The CCD camera used here is the Mutoh CV-16 CCD camera, which is the same one as we used at Norikura. We set up 2×2 binning, and subsequently the spatial resolution became 7.7'/pixel and the field of view was 98°×66°. We selected the exposure time as 20 *min*, and applied the filters of Hoya G-533 and Schott B. Unfortunately, we found that the exposure time in the case of Schott B filter was not enough to reduce the significant data. Therefore, we concentrated our analyses only on the data obtained by using the HOYA G-533 filter.

In this season, the position of the Gegenschein at midnight is near the place of the zenith angle $z \sim 20°$.. Consequently, the atmospheric extinction and the contamination by the airglow can be minimized. Moreover as the temperature of the open air was below -10 $°C$ at Kiso, we could keep by the refrigerator the favorable temperature of -30 $°C$ to reduce the dark noise largely on the CCD tip.

Both Kiso Observatory and Norikura Observatory are located in the direction of about 100km and 120km, respectively, north-east of Nagoya city. Therefore the similar contamination of city light in the low south-west sky, as noted in the observation at Norikura, appeared in the observation at Kiso. Furthermore we occasionally had a heavy snow in Kiso in February, 1997, and consequently the reflected light from the ground was not

negligibly small. Considering the contamination due to the city light and the weather condition, we found that the data obtained in the 5th March, 1997 are most reliable, and the available data for analysis cover $165° \leq \lambda - \lambda_{\odot} \leq 195°$, $-10° \leq \beta \leq 15°$.

2.3.3 Data reduction

In the ground observations, the observed intensity (I_{obs}) of the night sky is composed of those of starlight (I_{ST}), zodiacal light (I_{ZL}), airglow (I_{AG}), scattered light by lower atmosphere (I_{SL}) and the city light (I_{CL}).

$$I_{obs} = (I_{ST} + I_{ZL} + I_{AG}) \cdot e^{-\tau_{eff(z)}} + I_{SL} + I_{CL},$$

where $\tau_{eff(z)}$ denotes the optical depth of the atmosphere. We estimated $\tau_{eff(z)} \sim 0.10/cos(z)$ from the observations of a zenith angle z variation of the brightness of the reference stars. Especially main contamination in G band is OI airglow emission ($557.7nm$). Van Rhijn (1919) reported that this airglow has almost the uniform density layer. Therefore, we can approximate the brightness of airglow as a function of the zenith angle z.

The first step of the data reduction is flattening of the image frame. Fish-eye lens has its peculiar property, that is, the detected intensity in the center part of the frame is brighter than that in the edge of frame. In order to remove this effect, the raw data were divided by those detected for the flat field frame, which was acquired by taking the images of the fish tank filled with water and milk (a volume ratio of two components is about 10:1) as the similar method to that described in James *et al.* (1997). After this reduction, we removed the stars by using the computer program and smoothed the results. Almost all stars brighter than ~ 9 *mag* can be removed, except some bright objects such as planets of Jupiter, Saturn and Mars. The areas of CCD influenced by these bright objects, as well as by the background field stars in the Milky Way were smoothed computationally. A contribution from the stars fainter than ~ 9 *mag* is sufficiently low, *i.e.* below the noise caused by dark current.

The residual components of contamination are those due to airglow and city light. To determine the Van Rhijn function, we fit the minimum values of each zenith distance to arbitrary exponential function, and subtract the smoothed data by its function in order to find out the enhanced region by back scattering. The isophote maps of the reduced data are shown in Fig.9 for that obtained at Norikura, and in Fig.10 at Kiso.

2.3.4 Results

It is clear that the shape of the Gegenschein changes with the season (see Fig.9 and Fig.10). In addition, a center position of the maximum brightness of the Gegenschein deviates to the south in September and to the north in March. We have estimated the amount of the deviation, *i.e.* the latitude of the Gegenschein becomes about -0.°4 in September 1996 and +0.°7 in March 1997, while its longitude is nearly the same as the anti-solar point (see Table 1). For reference, the result obtained by the cooled CCD camera at Haleakala (altitude $3000m$, Hawaii, USA) (James *et al.* 1997), -2.°5 in September 1995 is also listed in Table 1. Observations of the latitude of the Gegenschein by various photoelectric and photographic observers compiled by Roosen (1970) have been shown in Fig.11, including three data listed in Table 1.

The north-south deviation found in the observations can be explained by the zodiacal cloud model having a symmetric plane deviated toward the south in September and toward the north in March (see, *e.g.* Misconi 1981). The invariant plane of the solar system is one plausible candidate, as shown in Fig.11, but we need more data to discuss a time variation of such deviation.

It has been proposed by Hong and Kwon (1991) that if the observed resolution of the Gegenschein is better that $\sim 3°$, one could show to be different in the cloud models. Since our observations have provided the isophote maps with the resolution better than $0.°5$, they are available to compare with those predicted by the several cloud models to estimate the structure of the zodiacal cloud.

We could not estimate the absolute brightness because of unremovable contamination by dark noise in CCD and OI airglow. By using the filters which can exclude the airglow, as well as more sensitive CCD camera, we will obtain the information of absolute brightness in our future observations.

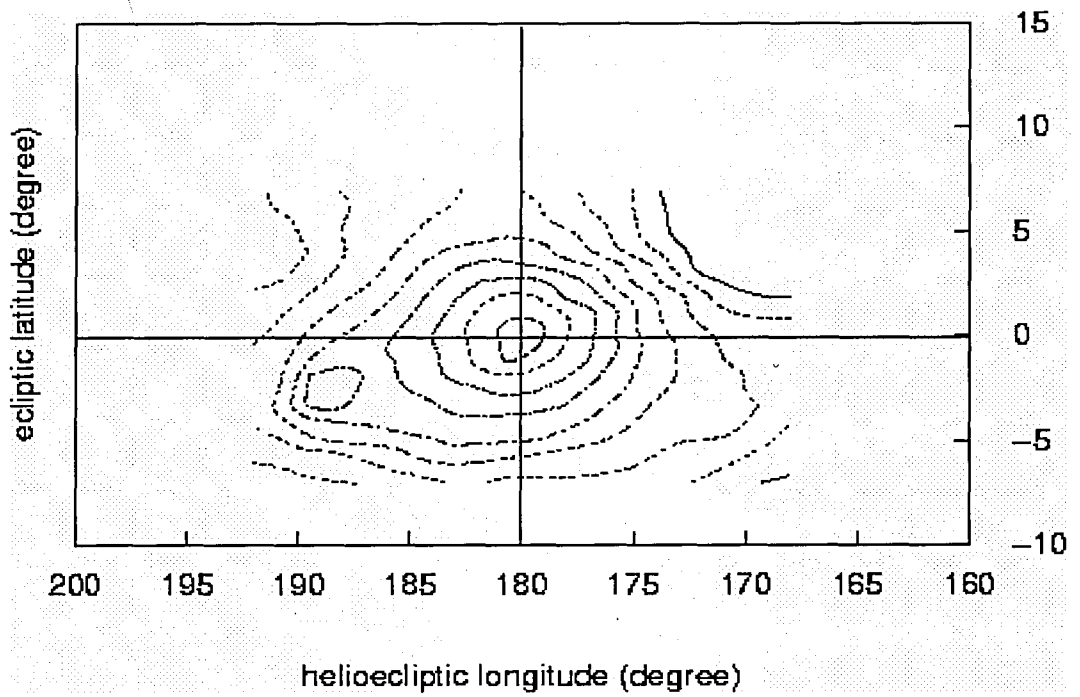

Figure 9: The isophote map, in arbitrary units, of the Gegenschein in Sept. 18, 1996 at Norikura. A slight hump in the left-down side is a residue of the effect of Jupiter due to incomplete deletion.

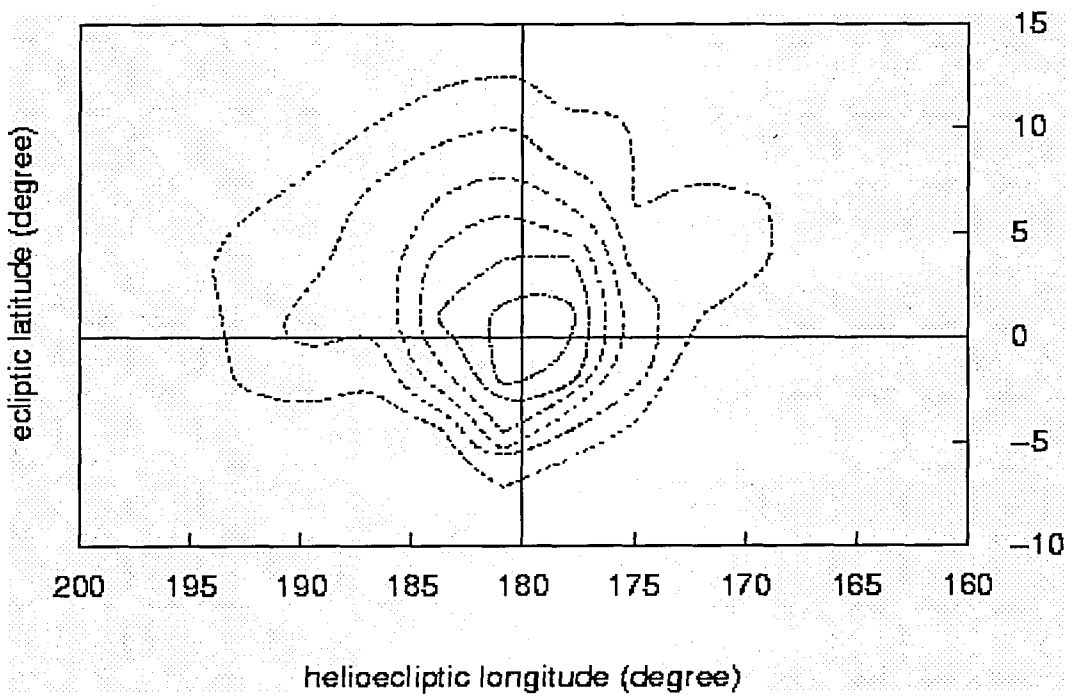

Figure 10: The isophote map, in arbitrary units, of the Gegenschein in March 5, 1997 at Kiso.

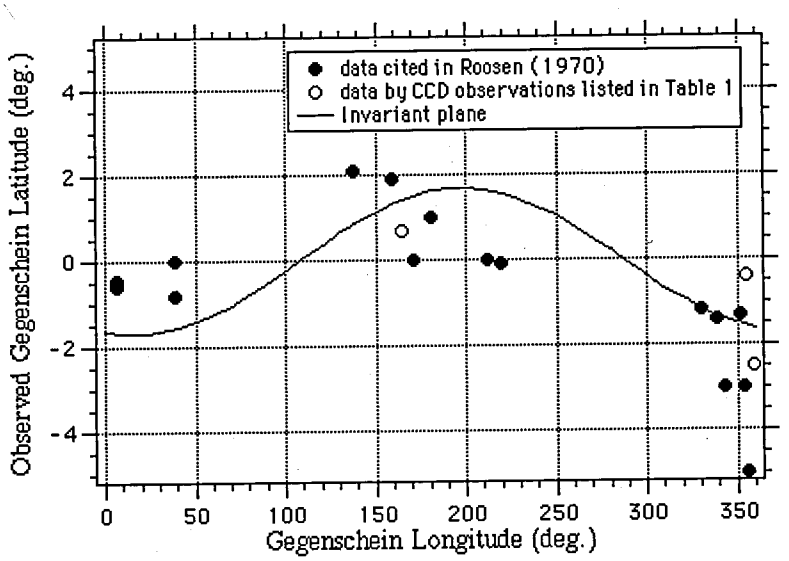

Figure 11: Observed position of the maximum intensity of the excess brightness (the Gegenschein) near the antisolar point.

site	date	North-South deviation (deg.)	East-West deviation (deg.)
Haleakala[1]	1995.9.22	-2.5	± 0
Norikura[2]	1996.9.18	-0.4	± 0
Kiso[2]	1997.3. 5	+0.7	± 0

Table 1. The position of the maximum brightness deduced from CCD observations near the antisolar point. ((1) James et al. (1997), (2) This paper)

3 First Detection of Visible Zodiacal Dust Bands from the Ground-based Observations*[4]

3.1 Introduction

Discovery of the interplanetary dust bands in observations by the Infrared Astronomical Satellite (IRAS) (Low *et al* 1984) has introduced the new concept that the zodiacal cloud has an inhomogeneous structure. In particular, prominent dust bands have been seen at ecliptic latitudes β of $\pm$ 10° (outer bands) and $\pm$ 1.°4 (inner bands). Analyzing the data obtained by the Diffuse Infrared Background Experiment (DIRBE), Reach *et al.* (1997) have reported the presence of additional faint dust bands at $\beta = \pm$ 6°, $\pm$ 13° and $\pm$ 17°, while Spiesman *et al.* (1995) have shown the first evidence of the scattered sunlight from the dust band particles.

It has been difficult to derive the brightness distribution of the zodiacal light from ground-based observations, not only because of its faintness, but also because of contamination by several kinds of diffuse light sources, such as the airglow and the light scattered by the lower atmosphere. However, recent CCD observations at higher altitudes have demonstrated the ability to measure the zodiacal light accurately (see, *e.g.* James *et al.* 1997 and Ishiguro *et al.* 1998).

An angular resolution of our instrument is 2.5′/pixel, which is higher than that of 0.°5 in IRAS low-resolution scans and 0.°7 in DIRBE, and is comparable to 2.0′/pixel in unfiltered IRAS high-resolution images. A further advantage of observing from the ground is that the zodiacal light over a wide range of solar elongation ϵ can be covered at any time of the year. Our observations were made in the region $75° \leq \epsilon \leq 180°$ at a solar ecliptic longitude of 220°, while IRAS and DIRBE covered the ranges $60° \leq \epsilon \leq 120°$ and $64° \leq \epsilon \leq 124°$ respectively, during the duration of their missions.

3.2 Observations and Data Reduction

3.2.1 Observations

We observed the zodiacal light on Mauna Kea, Hawaii, between October 29 and November 2, 1997. A Mutoh CV-16 CCD camera was used with a Sigma wide angle lens ($f = 24mm$, F=2.8). With a 2×2 binning, the angular resolution was 2.5′/pixel, and the field of view was 32° × 21°. To reduce contamination from the airglow, we used a Hoya B-390 filter with an IR cut filter. With this setup, the effective wavelength of our optics was 440 nm, and the full width at half maximum of the bandpass was 60 nm. The exposure time was set to 10 *minutes*, and the temperature of the CCD chip was kept at -19°C.

In the following analysis, we considered only the data obtained at Hale Pohaku (altitude of 2800m) on November 2. These consist of five sequences of morning zodiacal light frames taken during $3^h18^m - 4^h9^m(HST)$, and one Gegenschein frame taken during $1^h34^m - 2^h14^m(HST)$. To check the dark and readout noise during these observations,

[4]Adapted from Ishiguro et al. (1999a)

the 17 dark frames were obtained throughout the night.

When the wide angle lens was used, the light intensity at the edge of the frame became considerably less than that near the center. This effect and the pixel-to-pixel variations in sensitivity were removed by flat-fielding, using frames of a uniformly illuminated calibration source, which were taken inside the Integrating Sphere in the National Institute of Polar Research (NIPR), Tokyo, Japan, by the same instrument as used on Mauna Kea. The error in the absolute flux of calibration radiation inside the Integrating Sphere is less than 5 %. Transformation from pixel to ecliptic coordinates was described by a stereographic projection.

3.2.2 Data Reduction

On a moonless night, the observed sky brightness (I_{obs}) consists of light from several different sources, *i.e.* zodiacal light (I_{ZL}), airglow from the upper atmosphere (I_{AG}), the integrated starlight of unresolved stars (I_{ISL}), and the light scattered by the Earth's atmosphere (I_{sca}). That is,

$$I_{obs} = (I_{ZL} + I_{AG} + I_{ISL}) \cdot e^{-\tau_{eff}(z)} + I_{sca} \qquad (1)$$

where $\tau_{eff}(z)$ denotes the effective optical depth for the extinction of diffuse light sources at zenith distance z. The optical depth $\tau(z)$ for point sources is estimated by photometry of standard stars with magnitudes m_v between -1.5 and 6, where the magnitudes are taken from the 5th revised edition of the Bright Star Catalogue. A relation of $\tau(z)=0.19/\cos(z)$ is obtained. We estimate $\tau_{eff}(z)$ by using the empirical formula $\tau_{eff}(z) \simeq 0.75\ \tau(z)$ (Hong *et al.* 1998). The I_{ISL} is calculated by interpolating Pioneer's data cited in Leinert *et al.* (1998), and the I_{sca} comes from the formulae cited in Staude (1975). The most important contribution from I_{AG} is deduced from the van Rhijn function (van Rhijn 1919). Assuming that I_{AG} at $z=0$ is 100 $S_{10\odot}$, and that 1 ADU at $440nm$ on our instruments is equal to 3.2 $S_{10\odot}$ at $500nm$, we find perfect agreement between our data and the table for I_{ZL} in Leinert *et al.* (1998).

3.3 Results and Discussion

3.3.1 Parallactic distance of the dust bands

After removing stars and other diffuse light sources, we take a 24×24 *pixels* (1° × 1°) running average for the morning zodiacal light frames. Consequently, the fluctuation of the sky brightness across the CCD, mainly caused by photon noise and dark current, is reduced to less than 0.99 $S_{10\odot}$ for the morning zodiacal light, and less than 0.88 $S_{10\odot}$ for the Gegenshein. Fig.12a clearly shows the bumps around $\beta = 0°$, 3° and ±10°. The smooth background component has been fitted by a fourth order polynomial and subtracted from our observations. The lower curve indicates the existence of the inner and outer bands as residuals.

We employ Fourier filters similar to those described in Reach *et al.* (1997) to deduce the positions of the dust bands objectively. The original profile I_{ZL} is transformed into the filtered profile I_F by

$$I_F = \mathcal{F}^{-1}[\mathcal{F}(I_{ZL})exp(-f^2/2f_S^2)(1 - exp(-f^4/f_N^4))] \quad (2)$$

where $\mathcal{F}$ and $\mathcal{F}^{-1}$ denote the Fourier and inverse transforms, respectively. This technique enhances structures with angular scales between f_S^{-1} and f_N^{-1}.

Fig.12b shows the Fourier-filtered profile I_F of the morning zodiacal light with $f_S^{-1} = 3°$ and $f_N^{-1} = 10°$ (filter-I). Four prominent dust bands can be seen, and the profile is quite similar to the lower curve in Fig. 1a. We find additional faint structures near β=$\pm$5°, which may correspond to the A and B trails suggested in Sykes (1988), or to the $\pm$6° dust bands reported in Reach *et al.* (1997). Changing f_S^{-1} from 7° to 10° (filter-II), on Fig.14 we plot the three-dimensional profile of I_F. The separation between the bands near +10° and -10° is derived from multiple Gaussian fits to the latitude profiles (Fig.13). The fitting curve is adopted from the equations in a paper by Reach (1992). We find that the parallactic distance r of the bands is about 1.8 AU, and the separation Z between the bands is nearly 0.29 AU. It should be noted that our results depend on a "snapshot" of dust bands at a solar ecliptic longitude of 220°, and that Reach *et al.* (1997) estimated $r = (2.4 \pm 0.3)$ AU and $Z = (0.39 \pm 0.06)$ AU as the annual average. The parallactic distance is derived based on the assumption that the dust bands are due to the parallel rings of material. It should be noted that our visible observation is sensitive to the smaller dust particles, on which the Poynting-Robertson drag is more effective. Considering more realistic spatial distribution, such as migrating model recently developed by Reach *et al.* (1997), we may explain the disagreement of the parallactic distance between the infrared and visible observations as the difference of the effective size and/or the location of the observed interplanetary dust.

3.3.2 Gegenschein

A Fourier-filtered image of the Gegenschein shows 3 faint band structures almost parallel to the ecliptic plane (Fig.15). Their ecliptic latitudes are β=+2°, −4° and −9° for $165° \leq \lambda - \lambda_\odot \leq 185°$. Combining the measurements of the morning zodiacal light with those of the Gegenschein provides values of about 1.6 AU and 0.030 AU for R and Z respectively, where we have assumed that the inner dust bands observed in the morning zodiacal light correspond to the dust bands seen at β=+2° and −4° in the Gegenschein image. These values give a consistent brightness ratio of the inner dust band in the morning zodiacal light to that in the Gegenschein. Contrary to the outer bands, these results agree with those deduced from the DIRBE data by Reach *et al.* (1997), *i.e.* r=(1.7$\pm$0.2) AU and Z=(0.040$\pm$0.007) AU for the inner band pair.

The plane of symmetry of the zodiacal light is a useful concept to describe the interplanetary dust distribution and it provides us with important information on the origin and orbital evolution of interplanetary dust particles. Many space observations, both in visible and infrared, have been used to determine inclination and longitude of ascending node for the plane of symmetry (see, *e.g.*, Reach 1991). From ground-based observations of the Gegenschein (Tabane 1965), it is well known that the point of maximum brightness is displaced from the antisolar point to the north of the ecliptic plane in spring and the south in autumn. On the basis of recent CCD observations of the Gegenschein, Ishiguro *et al.* (1998) found that the plane of symmetry may coincide with the invariable plane of the solar system. In this work, however, we find the latitude of Gegenschein's center

is located at $+0.°3$ in contrast to the expected shift to the south in autumn. It is likely that the northern band structure shifts the position of the maximum brightness of the Gegenschein toward the north. In order to deduce the symmetry plane of the background zodiacal light accurately, we must carefully eliminate the effect of the inner dust bands.

3.4 Conclusions

We have confirmed the existence of the two dust band pairs seen in the morning zodiacal light. This is the first evidence from ground-based observations in visible light. In addition, three dust bands have been discovered around the antisolar point. Two of them are possibly extensions of the inner band pair. It should be emphasized that ground-based photometry of the zodiacal light, using a cooled CCD camera, has enabled us to investigate not only the entire structure of the dust bands, but also their spatial/temporal variations, such as those seen in the A and B dust trails. Our observations open the possibility of further advancing knowledge of the solar system dust cloud without the need of a space telescope.

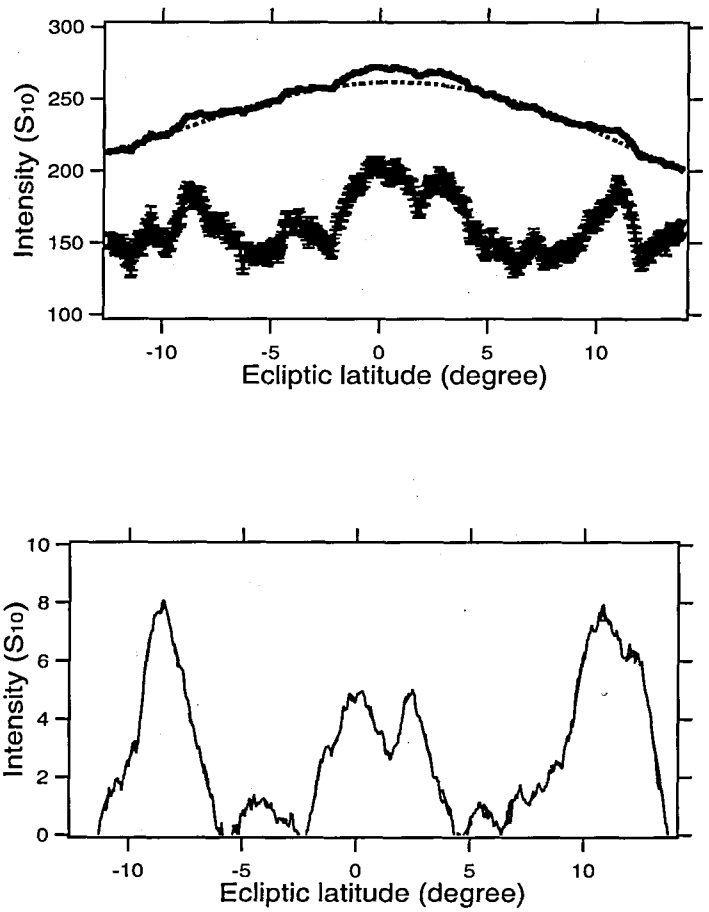

Figure 12: (a) Surface brightness profile of the morning zodiacal light at solar elongation of 78° ($\lambda - \lambda_\odot = 282°$). The data was taken at Mauna Kea, Hawaii during $3^h49^m - 3^h59^m(HST)$. The dotted line denotes the fit to the background component by a fourth order polynomial. The difference between the brightness profile and the smoothed background is indicated by the lower curve. For clarity, the lower curve and error bars are scaled by a factor of 5 and shifted by 150 $S_{10\odot}$. Prominent bands can be found at $\beta = 0°$, 3° and ±10°. (b) The Fourier-filtered surface brightness at solar elongation of 78° ($\lambda - \lambda_\odot = 282°$) with filter-I.

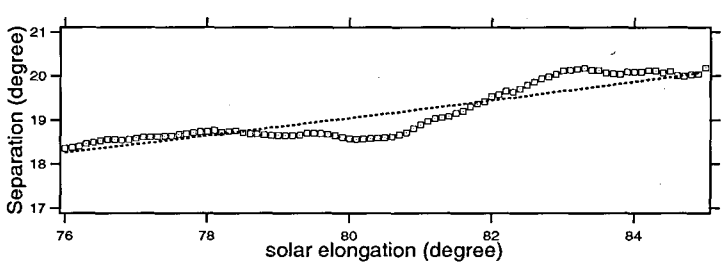

Figure 13: The separation between the ±10° band pair deduced from five Fourier-filtered profiles of the morning zodiacal light. The data have been averaged over 0.°1.

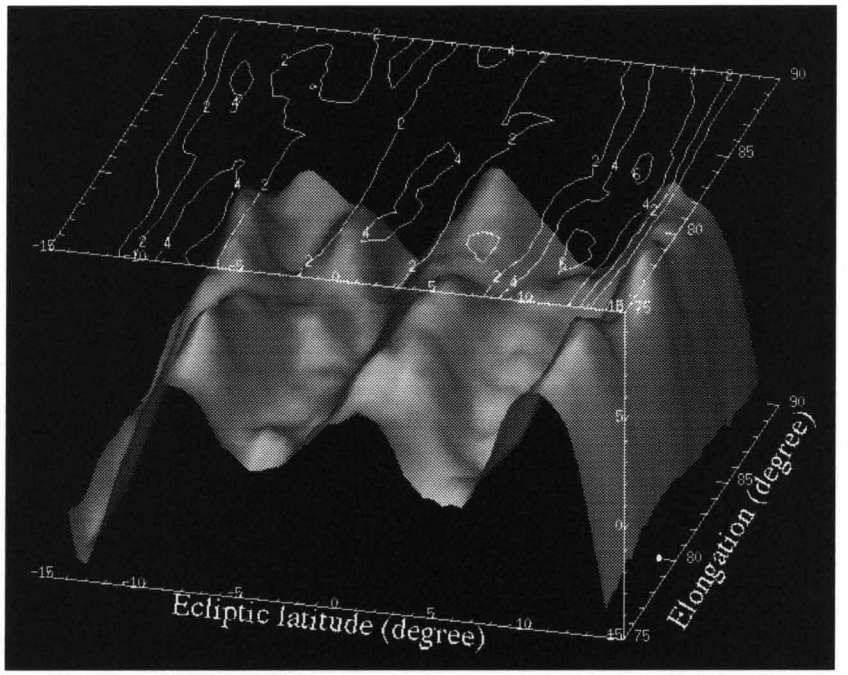

Figure 14: The three dimensional profile of I_F for the morning zodiacal light with filter-II, for the same data as in Fig.12b. The isophoto map of excess surface brightness is illustrated in the upper plane in units of $S_{10\odot}$.

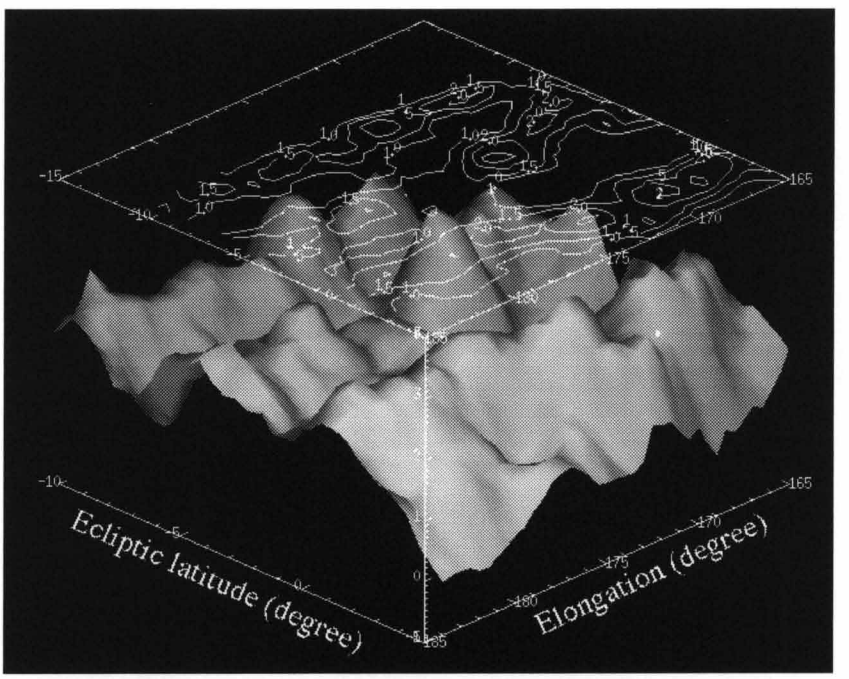

Figure 15: Same as Plate 1, but for the Gegenschein taken during $1^h34^m - 1^h44^m(HST)$. Three band structures at $\beta = +2°, -4°$ and $-9°$ are apparent.

4 Comparative Studies of Visible and IRAS interplanetary Dust Bands*[5]

4.1 Introduction

Infrared Astronomical Satellite (IRAS) has discovered asteroidal dust bands at the ecliptic latitude $\beta = \pm 1.^{\circ}4$ and $\beta = \pm 10^{\circ}$ (hereafter Themis/Koronis bands and Eos bands, respectively) (Low et al. 1984). It is widely accepted that both of them are associated with asteroidal families while the origin of weaker dust bands at $\beta = \pm 6^{\circ}$, $\pm 13^{\circ}$ and $\pm 17^{\circ}$, later identified by DIRBE (Reach et al. 1997), has not yet been clarified. Furthermore, several cometary dust trails (Sykes and Walker 1992) and a different type of dust trails with unknown origin (Type II) have also been observed (Sykes 1988). These discoveries brought us a new concept of the zodiacal dust clouds, i.e., the existence of many local structures in the zodiacal cloud complex directly associated with the source.

While it is generally believed that the asteroidal families were produced by the catastrophic disruption of the main-belt asteroid, there still remains a controversy on the model of subsequent formation of dust bands (Sykes et al. 1989). In any model, however, the dynamical evolution due to the Poynting-Robertson effect should be taken into account because the time scale to form the interplanetary dust torus by Jovian precession ($\sim 10^5 - 10^6 yrs$) is comparable to the Poynting-Robertson lifetime ($\sim 10^6 yrs$) of the band particles. Reach et al.(1997) have constructed the three-dimensional spatial distribution model, i.e. the migrating band model to account for not only the torus structure of dust bands, but also its dynamical evolution due to the Poynting-Robertson effect.

Recently, Ishiguro et al.(1999a, hereafter paper I) made the first detection of the visible dust bands from the ground-based observation. They have found that the dust bands exist not only in the region of solar elongation $270^{\circ} \leq \lambda - \lambda_{\odot} \leq 285^{\circ}$ ($75^{\circ} \leq \epsilon \leq 90^{\circ}$), which overlapps that observed by IRAS and DIRBE, but also near the anti-solar direction ($165^{\circ} \leq \lambda - \lambda_{\odot} \leq 185^{\circ}$). In paper I, the parallactic distance of dust bands has been derived based on the assumption that the dust bands found at $\beta = +2^{\circ}$ and -4° found around the anti-solar direction are the extension of inner dust bands seen at $\lambda - \lambda_{\odot} \sim 270^{\circ}$. In this paper, the validity of this assumption will be examined carefully through the model calculations based on the empirical migrating band model proposed by Reach et al.(1997).

4.2 Direct comparison between the visible and IR dust bands

The data in the visible wavelengths were obtained at Hale Pohaku on Mauna Kea between October 29 and November 2, 1997. After the sophisticated reduction procedures (see Paper I for the detail), we have confirmed the visible zodiacal dust bands at $\beta = 0^{\circ}$, 3° and $\pm 10^{\circ}$ in $270^{\circ} \leq \lambda - \lambda_{\odot} \leq 285^{\circ}$. Moreover, visible dust bands were discovered at $\beta = +2^{\circ}$, -4° and -9° in $165^{\circ} \leq \lambda - \lambda_{\odot} \leq 185^{\circ}$.

IRAS did a scan over the sky from a nearly polar orbit above the terminator of the Earth. The calibrated data of infrared dust bands with the resolution of $2.0'$ are available for the Zodiacal Observation History File (ZOHF) (IRAS Explanatory Supplement, 1988). To compare the visible and infrared dust bands observed at the same Earth's location (November 2), we used SOP 562 in ZOHF. Applying the same Fourier filter method to the

[5] Adapted from Ishiguro et al. (1999b)

visible and infrared data along the ecliptic latitude to enhance the dust band structure, we have obtained the latitude profiles of the visible and infrared dust bands at $\lambda - \lambda_\odot = 271°$ (see Fig.16). Although Themis/Koronis bands near $\beta = 0°$ can be resolved more clearly into a pair in the infrared wavelengths, its separation in the visible becomes weak. This may be caused by the differences in the spatial distribution of band particles observed in the visible and infrared wavelengths due to a size dependence of dynamical evolution of dust ejected from the parent asteroids. In addition, the $\beta = \pm 5°$ bands are present in the visible data, in contrast to little evidence in the infrared data, except the small bump at $\beta = 5°$ for the IRAS data of a wavelength of $\lambda_{WL} = 60 \mu m$. It should be noted that two observations were made on the same date of November 2, but the time interval is 15 years.

Fig.17 shows the energy distribution of $\beta = +10°$ dust band (Eos dust band) at $\epsilon = 90°$. The value at $\lambda_{WL} = 0.44 \mu m$ comes from our observation (Ishiguro et al. 1999a). Our visible observation does not conflict with the infrared results in Spiesman et al. (1995). Consequently, the visible albedo of Eos dust band particles is ~ 0.2 as derived in Spiesman et al. (1995) in the near infrared wavelengths. We found, therefore, that the color of Eos dust band is neutral or a bit redder in the visible and near infrared wavelengths. It is interesting to note that the color of the asteroids in Eos family is neutral or slightly redder in the visible (Doressoundiram et al.1997). It may support that the dust particles in the $\beta = +10°$ dust band come from the Eos family.

4.3 Model calculation of the dust bands around the anti-solar point

Due to the restricted configuration of infrared satellites' orbit, no infrared data are available around the anti-solar point. Then, we compare our visible observations with a model calculation in this section. Referring to the model for the spatial distribution of interplanetary dust bands, which was derived from the infrared data taken around $\lambda - \lambda_\odot = 270°$, we can theoretically predict the brightness profile of visible dust bands around the anti-solar point. The integrated brightness of the scattered light along a line of sight, $I(\beta)$, is represented by

$$I(\beta) = \int_0^\infty \frac{1}{r^2} F_0 \, n(r, Z) \, \phi(\Theta) \, dl, \tag{3}$$

where l denotes a geocentric distance of the dust particle, F_0 means the solar flux at a heliocentric distance $r = 1AU$, and Z is the height from the symmetric plane of the dust distribution (see Sykes 1990). We employ a linear combination of three Henyey-Greenstein functions as the mean volume scattering phase function $\phi(\Theta)$ (Hong 1985). The number density $n(r, z)$ of the dust particles in the dust bands is given by equation (3) in Reach et al.(1997), i.e.,

$$n(r, \zeta) = \frac{Ro}{r} \, e^{-\left(\frac{\zeta}{\delta_\zeta}\right)^6} \left(1 + \frac{1}{v_i}\left(\frac{\zeta}{\delta_\zeta}\right)^{p_i}\right), \tag{4}$$

where $\zeta \equiv Z/r$, and the parameters to adjust the shape of the dust bands are δ_ζ (a position of latitude peak), R_0 (a heliocentric distance of peak position), v_i (a central density) and p_i (a sharpness of latitude peak). It should be noted that we used the values of above parameters given in Reach at al. (1997) which were derived to fit the model

calculation to the band structures detected by IRAS. In addition, it has been implicitly assumed that the dust grains existing in the inner dust bands came from the catastrophic events related to the origin of the Themis and Koronis families. We applied the filtering procedure after adding the smooth background profile to the band structure (Grogan et al. 1997 ; Dermott et al. 1994a). Fig.18 shows the intensity distribution of dust bands filtered at $\lambda - \lambda_\odot = 173°$. The model calculation (dotted curve) shows a fairly good fit to the observed position and relative intensities of the Themis/Koronis bands (solid curve) at $\beta = +2°$ and $-4°$. It is concluded, therefore, that the two dust bands, observed around the anti-solar point, are the extension of the Themis/Koronis dust bands found by IRAS. Furthermore, their apparent separation is widened with increasing the solar elongation by a simple geometric effect. For this reason, Eos bands are out of range covered by our observations at the antisolar point.

It should be noted that the question of why the discrepancy between the intensities of model calculation and observation at $\beta = -10°$ appears in Fig.18 is not directly addressed by our model, because its application is limited to the analysis of the inner dust bands alone.

4.4 Conclusions

We have calculated the visible intensity distribution of the dust bands near the anti-solar direction by using the migrating band model. Although the model was originally developed to fit the infrared observations around $\epsilon = 90°$, it is found that the resulting peak positions and relative intensities of dust bands at $\beta = +2°$ and $-4°$ near the anti-solar point show good agreements with the visible observed evidence. Therefore, we can conclude that our previous assumption in Paper I has been confirmed, i.e., the visible dust bands found at $\beta = +2°$ and $-4°$ near the anti-solar point are the part of the dust bands discovered by IRAS at $\epsilon = 90°$ as Themis/Koronis dust bands.

In principle, the size of dust particles responsible for the scattered light is different from that dominating the thermal infrared radiation. Actually, we reported the disagreement between the parallactic distance of visible dust bands and infrared dust bands in paper I. This conclusion was derived from the assumption that the parallactic distance depends on a simpler ring-pair model. On the other hand, the migrating model used here gives more realistic description of the dust spatial distribution. Resulting fair good agreement between the visible and infrared profiles in $\lambda - \lambda_\odot \sim 270°$ suggests that the spatial distribution of dust bands is not so sensitive to the size of dust particles. This result validates to derive the albedo of dust particles existing in the bands (Spiesman et al. 1995).

A remaining problem in the comparative studies of infrared and visible dust bands is an appearance of visible dust bands at $\beta = \pm 5°$ in $\lambda - \lambda_\odot \sim 270°$, in contrast to no hump in the infrared data. Furthermore, the origin of $\beta = -10°$ dust band found in the visible near the anti-solar point is still unknown. One possibility is that $\beta = \pm 5°$ bands may correspond to the parent-unknown dust bands observed at $\beta = \pm 6°$ by DIRBE (Reach et al. 1997), and the $\beta = -10°$ band seen in the visible in $\lambda - \lambda_\odot \sim 180°$ may be their extension. Unfortunately the spatial coverage of our data was not sufficient to confirm this hypothesis directly. In addition, no model parameters are available from the infrared observations due to the faintness of $\beta = \pm 6°$ bands in the infrared. Alternatively, they might be partial or temporary dust bands (Type II) reported in Sykes and Walker (1992).

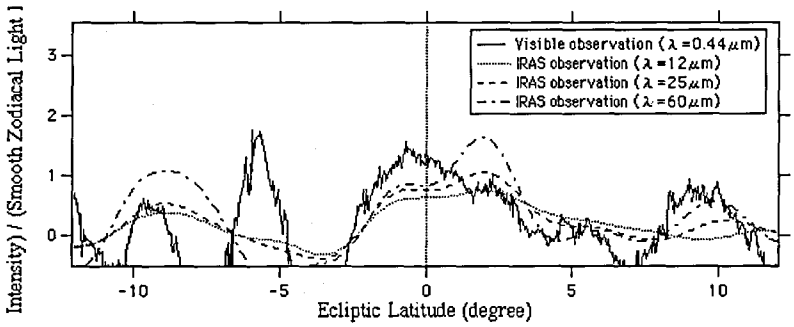

Figure 16: Relative intensity of dust bands filtered along the ecliptic latitude at a helioecliptic longitude of $\lambda - \lambda_\odot = 271°$ ($\epsilon = 89°$), where the data came from Ishiguro et al. (1999a, Paper I) in the visible and ZOHF in IRAS.

If so, we may observe their motion along the orbit from the continuous observations. The further ground-based observations in the visible will unveil the nature of such mysterious dust bands in the near future.

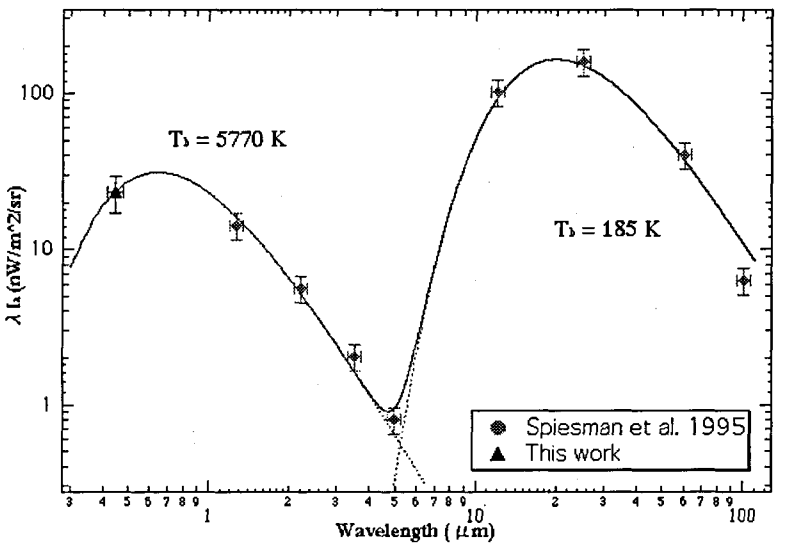

Figure 17: The energy spectrum of the $\beta = +10°$ dust band at 90° elongation. Infrared data(open circles) are obtained by DIRBE observations (Spiesman et al. 1995). A filled triangle represents our visible data given in Ishiguro et al. (1999a). Two solid curves indicate the sum of 5770K and 185K black body curves, and dotted curves show each components.

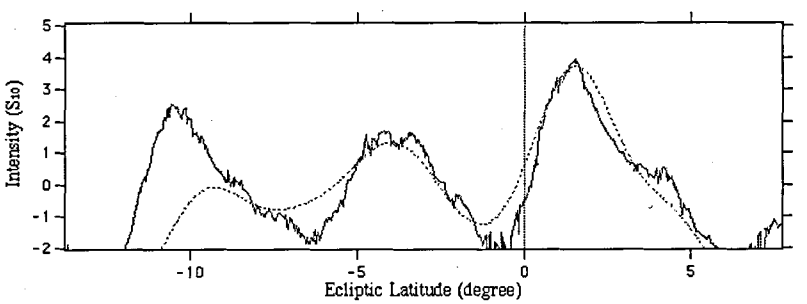

Figure 18: Intensity distribution of dust bands filtered at a solar elongation of $\lambda - \lambda_\odot = 173°$. Solid and dashed curves denote, respectively, the observed data by Ishiguro et al. (1999a, Paper I) and the calculated results based on the migration model in the text.

5 Fade-out of Eos dust bands below helioecliptic longitudes of 60° and the detection of a wide Encke dust trail in the visible wavelengths*[6]

5.1 Introduction

In the so-called equilibrium model, dust bands are presumed to be formed as a result of the continual erosion of asteroids in the asteroid belt due to impacts by interplanetary meteors (Dermott et al. 1984). On the other hand, Sykes and Greenberg (1986) proposed a catastrophic model, in which the dust was supplied by the break-up of collisional fragments from a single ancient asteroidal collision that generated the asteroidal family. Although the origin of the dust bands is still unknown, it is widely believed that the dust particles in the asteroid belt disperse due to their kinetic energies and simultaneously spiral towards the Sun due to Poynting-Robertson drag forces. The orbits precess due to Jovian perturbations, and consequently the orbital nodes spread across all longitudes after $\sim 10^7$yr (Sykes and Greenberg 1986). The resulting spatial distribution of such particles looks like a torus (see e.g. Sykes 1990).

If the catastrophic disruption occurred recently, the particles in the catastrophic model might not have been transported into the inner region of the solar system. Consequently, the bands would not extend across all ecliptic longitudes. Furthermore, other physical processes play important roles in the dynamical evolution of band structure during the transportation of dust particles into the inner solar system. These processes include the planetary perturbation of the inner planets (see e.g., Gustafson et al. 1987 and Dermott et al. 1992) and dust-dust collisions (see e.g. Grün et al. 1985 and Ishimoto 1998). The Lorenz force (Mukai & Giese 1984) may also influence the resulting band structure and its time variation.

The first detection of interplanetary dust bands in the visible wavelengths by Ishiguro et al. (1999a, hereafter Paper I) demonstrated the possibility of studying the complex spatial structure of the interplanetary dust cloud from ground-based observations. We performed further observations of the zodiacal light in November and December 1998, at the summit of Mauna Kea, Hawaii, using the same instruments as used in 1997 (Paper I), but applying an improved filter, as shown later. The aim of this paper is to describe the new findings obtained by these observations.

The first scientific objective of the present observations is to examine the dynamical evolution of the bands of dust that come from the Themis, Koronis and Eos families of asteroids. The findings will be based on data collected at as small a helioecliptic longitude ϵ as possible.

In addition to the dust bands associated with the three most prominent asteroid families, observations by the IRAS satellite also found three types of structure. They are (i) fainter structures related to the Maria and Eunomia/Io families (Reach et al. 1997), (ii) cometary dust trails (see, e.g. Sykes 1986), and (iii) extended bands of unknown origin (Sykes 1988). The second scientific objective of our present observations is to confirm the existence of such faint structures, and to study their origin and dynamical evolution.

Our observations and data analyses are described in section 5.2. The findings of the observations are summarized in section 5.3.1, and the procedures for modeling the band

[6]Adapted from Ishiguro et al. (1999, Submitted to ApJ)

structures are described in section 5.3.2. In section 5.4, we discuss the fade-out of the Eos dust bands that were found. A summary is presented in section 5.5.

5.2 Observations and Data Analysis

In this paper, we present the results of zodiacal light observations conducted at the summit of Mauna Kea, Hawaii on 15 December 1998. Our instruments consisted of a Mutoh CV-16 cooled CCD camera attached to a Nikon fish-eye lens (f=16mm, F=2.8). We have developed a special filter to reduce airglow contamination. As shown in Fig.19 , there are no prominent airglow emission lines in the wavelength region transmitted by this filter. Since we use the CCD camera without binning, the angular resolution is $2.0'$/pixel. The effective wavelength of our optics is $500nm$, and the bandpass is between 439 and $524nm$. The exposure time was set to 10 minutes, and the temperature of the CCD chip was kept at $-30°C$ during the whole observation period. Twenty-seven dark frames were obtained throughout the night to check the dark and read-out noise.

By observing the night sky at zenith using the new filter, we deduced the intensity of airglow there to be 41 $S_{10_\odot}$, where 1 $S_{10_\odot}$ at $500nm = 1.28 \times 10^{-8} Wm^{-2} sr^{-1} \mu m^{-1}$. This intensity is half that measured during our previous observation using a filter with an effective wavelength of $440nm$ and a bandpass FWHM of $60nm$ (Paper I). Although the intensity of the airglow varies with time, the improved filter is expected to reduce contamination.

We report here the results of the evening data alone (i.e., in the trailing side of the Earth's orbit). The available data cover two regions of the sky. The first set of data is a combination of six frames in the region $50° \leq \lambda - \lambda_\odot \leq 85°$ and $-25° \leq \beta \leq 25°$ ($19^h14^m - 20^h18^m$ (HST)), and the other is a combination of six frames in the region $85° \leq \lambda - \lambda_\odot \leq 120°$ and $-25° \leq \beta \leq 25°$ ($20^h32^m - 21^h25^m$ (HST)). There is no significant contamination by galactic light in either set, because of the high galactic latitudes of $35° < |b| < 85°$.

The data reduction methods to subtract the fish-eye lens effects and the atmospheric diffuse light were described in detail in Paper I. From the photometry of solar analog stars, we find that 1 ADU on our instrument corresponds to 3.1 $S_{10_\odot}$.

Applying different sets of Fourier filters, we separate the observed intensity of the zodiacal light ($=I_{obs}$) into three different components: the smooth background cloud I_{smooth}, the band structure I_{band}, and the high frequency noise component I_{noise}, caused mainly by starlight and by dark and photon noise.

$$I_{smooth} = \mathcal{F}^{-1}[\mathcal{F}(I_{obs})\ exp(10000 * (f - f_S))] \tag{5}$$

$$I_{noise} = \mathcal{F}^{-1}[\mathcal{F}(I_{obs})\ exp(-10000 * (f - f_N))] \tag{6}$$

$$I_{band} = I_{obs} - I_{smooth} - I_{noise}, \tag{7}$$

where $\mathcal{F}$ and $\mathcal{F}^{-1}$ denote Fourier and inverse Fourier transformations, respectively. This technique enhances structures with angular scales f^{-1} between f_S^{-1} and f_N^{-1}. In this paper, we set the parameters $f_N^{-1} = 5°$ and $f_S^{-1} = 20°$. We then employ a 15 pixel (0.5°) running average along ecliptic latitudes.

5.3 Results and Model calculations

5.3.1 Extracted structures

The image of the dust bands detected on 15 December 1998 is shown in Fig.20, after Fourier filtering. It is clear that the Themis/Koronis dust bands exist around $\beta \sim 0°$, and become brighter at lower helioecliptic longitudes. On the other hand, the Eos dust bands seen around $\beta = \pm 10°$ become fainter with decreasing helioecliptic longitude $\lambda - \lambda_\odot$, and finally fade out at $\lambda - \lambda_\odot \leq 60°$. In Fig.21, we plot the peak intensities of both bands as a function of helioecliptic longitude. For the Eos dust bands, the intensity is derived from summing the intensities of the south/north bands. The error in the intensity is found to be less than 2 $S_{10_\odot}$.

It should be mentioned that we found other significant features (see Fig.20). Namely, (i) a faint bump around $\beta = \pm 17°$, $90° \leq \lambda - \lambda_\odot \leq 120°$ may be the dust band associated with the Maria asteroidal family, reported by Reach et al. (1997). (ii) An extended band structure appears in the region of $15° \leq \beta \leq 25°$ and $50° \leq \epsilon \leq 70°$. Since it is not parallel to the ecliptic plane, it is highly probable that this is a dust feature similar to the cometary dust trails detected by IRAS (Sykes 1986). Our preliminary analysis, shown later, suggests that this feature is associated with comet P/Encke.

The lack of evidence for the $\beta = \pm 5°$ bands in the present observations, in contrast with their existence in the 1997 observations (see Paper I), leads to the conclusion that they were either partial or temporary dust bands, as discussed in Ishiguro et al. (1999b).

5.3.2 Modeling the dust bands

(I) Interplanetary dust bands

We focus our analyses on the dust band structures associated with the three asteroidal families Themis, Koronis and Eos, because the band associated with the Maria family is too faint for a proper detailed analysis.

To compare the intensity distributions of the observed dust bands (I_{obs}) with those of model calculations, we use a dust band model that incorporates 2 elements. These are the toroidal distribution of the dust particles, as deduced from the orbital elements of the asteroidal families, and the expected transportation of particles into the inner Solar System by Poynting-Robertson drag. The basic ideas and assumptions behind our model calculations are as follows:

(i) The dust particles in the band have mean proper orbital elements equivalent to those of the members of the parent asteroid family. The dispersion in the orbital inclination (di) is a free parameter. The orbital eccentricities of the dust particles are assumed to be zero.

(ii) The dust band particle population has a number density proportional to $1/r$ (where r denotes the heliocentric distance), and its distribution is derived from a simple Poynting-Robertson drag.

(iii) The force elements (i_f, Ω_f) are taken from Dermott et al (1992), where i_f and Ω_f correspond, respectively, to an inclination and an ascending node of the midplane of the dust cloud with respect to the ecliptic plane. That is, we use the relationships $i_f = 4.85° - 2.86° \times r + 0.55° \times r^2, \Omega_f = 31.91° + 21.69° \times r$ for the Eos dust bands (r is in units of AU), and $i_f = 4.73° - 2.82° \times r + 0.55° \times r^2, \Omega_f = 33.60° + 20.40° \times r$ for the Themis/Koronis dust bands.

(iv) Once the spatial distribution of the band particles is specified, the observed brightness of the dust bands is calculated by integrating along the line of sight. To calculate the mean volume scattering phase function, a linear combination of three Henyey-Greenstein functions proposed by Hong (1985) is employed. The total observed brightness of the zodiacal light consists of two components: that from the dust bands and that from the smoothed interplanetary dust cloud. Following Grogan et al.(1997), we employ an iterative method to estimate the bands' observed brightness from the modeled sum of these two components.

First, the dispersion *di* in the proper orbital inclination is set to be a constant value (the 'constant model'), i.e., *di*=0.3° for the Themis bands, 0.1° for the Koronis bands, and 1.0° for the Eos bands. These values give the best fit to the observed dust bands' intensity profile along ecliptic latitude β at $\lambda - \lambda_\odot = 90°$. As shown in Table 2, these values of *di* are similar to those estimated from infrared observations. These findings are consistent with the results shown in Ishiguro et al.(1999b): the latitude profile of the visible dust bands at $\lambda - \lambda_\odot = 271°$ ($\epsilon = 89°$) is similar to that of the infrared dust bands. In addition, the dust band model deduced from the infrared observations can predict the visible band structure near the anti-solar point detected in Paper 1.

We find in Fig.21 that the peak intensity along helioecliptic longitude $\lambda - \lambda_\odot$, derived from the model calculations for the Themis/Koronis bands, agrees well with those observed in the entire $\lambda - \lambda_\odot > 50°$ region.

The model peak intensity profile along $\lambda - \lambda_\odot$ of the Eos bands, however, looks quite different from that observed at $\lambda - \lambda_\odot < 70°$. That is, the 'constant model' for the Eos dust bands yields an increasing intensity with decreasing $\lambda - \lambda_\odot$, against the observational evidence. It is known (see, e.g. Grogan et al. 1997) that as the dispersion increases, the contrast between the number density of the band particles at the peak and at the center becomes weaker. This suggests that variation of *di* with solar distance *r* might reduce the peak intensity of band structures near the Sun. Therefore, for the Eos dust bands, we use a simple model for the dust band structure with the *r*-dependence of *di* given in Table 2 (we call this the 'variable model').

The solid curve in Fig.21 shows the result based on this 'variable model'. It is found that an increasing *di* with decreasing *r* for the Eos bands can predict the fade-out of the Eos dust bands near the Sun.

(II) Cometary dust trail

As shown in Fig.20, a faint extended feature appears in the region $15° \leq \beta \leq 25°$ and $50° \leq \lambda - \lambda_\odot \leq 70°$. Its brightness is nearly 5 $S_{10_\odot}$, and its width is about 5°, which corresponds to about 0.03 AU at the orbit of comet P/Encke as seen from the Earth. In Fig.22. we illustrate the position of a tube with a radius of 0.015 AU along the orbit of comet P/Encke. Its position fits quite well to that of the observed feature. We apply a simple model for the dust cloud inside the tube. Namely, we assume the dust particles have a uniform radius of $100\mu m$, an albedo of 0.1, and a number density of $9 \times 10^{-11} particles\ m^{-3}$. Mukai (1989) has shown that dust particles ejected from comet P/Encke with radii larger than $5\mu m$ can stay in the solar system, despite the solar radiation pressure on them, although their resulting orbits after leaving the parent comet have not been investigated in detail.

The computed brightness expected at the center of the tube is shown in Fig.22, where a scattering function the same as that for the dust bands has been used. The Eos dust

band overlaps the tube at the corner of the tube. In addition, the lower part of the tube is not visible because it is too faint, as calculated in Fig.22, and is located in the Themis/Koronis dust bands. Consequently, we suppose that only the part of the tube that is far from the ecliptic plane appears in our observations.

It should be noted that the width of the dust trail detected in our observations, *i.e.*, 0.03 AU $\sim 4.5 \times 10^6 km$, is larger than that estimated from infrared observations. Sykes and Walker (1992) derived a width of about $(680 \pm 71) \times 10^3 km$ from the IRAS data, and Reach et al. (1999) deduced the size of the central core as $2 \times 10^4 km$ from the ISO data. In the visible wavelengths, smaller dust particles are the dominant contributors to the brightness of dust trails, whereas larger particles are the dominant contributors to infrared emission. In general, smaller particles are spread more widely from the original orbit of the parent comet. This may be why the visible trail is wider. In addition, the width may vary along the trail as the distance from the parent comet changes. Infrared trails have been detected near the parent comet, while we find the relatively wider dust trail is far from comet P/Encke, as illustrated in Fig.23. Further observations in the visible wavelengths, especially near the comet, are greatly needed.

5.4 Discussion

From our new observations of interplanetary dust bands, it has been found that the Eos bands are not seen below a helioecliptic longitude $\lambda - \lambda_\odot \leq 60°$. The migration band model derived from the infrared observations of Reach et al.(1997), which corresponds to the 'constant model' in our treatment, suggests that the intensity of each band increases toward the Sun, as detected for the Themis/Koronis dust bands in Fig.21. We have shown that the original migration model is not appropriate for explaining the fade-out of the Eos bands. Therefore in section 5.3.2 (I). we have proposed the 'variable model' for band structure, where the dispersion in the orbital inclinations di of the band particles increases as the particles approach the Sun, and the number density of the particles falls below the observable threshold.

The first question that we have to ask is why the dust particles composed of asteroidal dust show such an increase of di with a decrease in heliocentric distance? The collision of dust particles (*e.g.*, impacts with interplanetary dust as well as with interstellar dust and β-meteoroids) is one of the potential physical processes that may increase the dispersion in the orbital inclinations of band particles. It is well known that collisions of dust particles become dominant near the Sun (*e.g.* Ishimoto 1998). The loss of the small collisional debris from the dust bands, due to solar radiation pressure, is a welcome process, reducing the number density of band particles near the Sun. The Lorenz force exerted by the interplanetary magnetic field on the charged dust particles may also accelerate the dispersion in the orbital inclinations of the dust particles, as discussed in Mukai & Giese (1984).

The second question is why a fade-out does not occur in the Themis/Koronis dust bands, in contrast with that found in the Eos dust bands? It has been predicted that in the competition between production and loss of band particles in a dust band torus, gradual loss eventually wins out with time (Sykes and Greenberg 1986). The minimum age of asteroid family formation estimated by Sykes et al. (1989) suggests that the Eos family is the oldest among the three major families, i.e. Themis ($1.5 \times 10^6 yr$), Koronis ($1.3 \times 10^8 yr$) and Eos ($5.8 \times 10^8 yr$). If the estimated formation times of the dust bands are

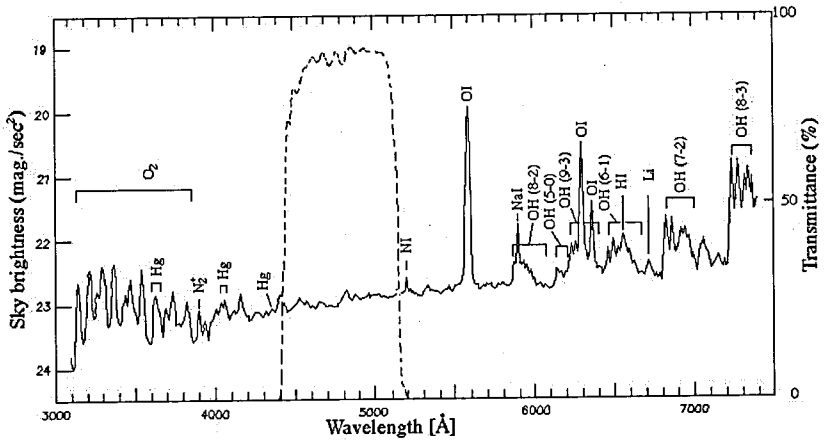

Figure 19: The transmission spectrum of the filter used in this observation. To learn the emission spectrum of the airglow, we refer to the average sky brightness at zenith as a function of a wavelength (CFHT Observers' Manual).

correct, the Eos dust bands may already have entered the fading phase, where dust loss is dominant. The loss of band particles due to comminution of collisional debris occurs preferentially in the inner Solar System. As a result, the Eos dust bands may fade away near the Sun.

5.5 Summary

We present the results of our recent observations of interplanetary dust bands, conducted at the summit of Mauna Kea on 15 December 1998. It is found that (1) the increase in the peak brightness of the band structures associated with the Themis and Koronis families occurs from helioecliptic longitude $\lambda - \lambda_\odot$ of 120° to 50°. In contrast, (2) the Eos dust bands fade out in the region of $\lambda - \lambda_\odot \leq 60°$. Such a fade-out suggests that loss of band particles is the dominant process in the Eos dust bands. (3) The dust trail associated with comet P/Encke has been found in the visible wavelengths for the first time. We find that the visible trail is significantly wider than the infrared trail. (4) The band structures detected at $\beta = \pm 5°$ on 2 November 1997 could not be seen on 15 December 1998. This suggests that the dust bands at $\beta = \pm 5°$ had either a partial or a temporary structure. We shall perform further observations to examine such partial structures in the interplanetary dust bands, as well as other inhomogeneous structures in the zodiacal cloud.

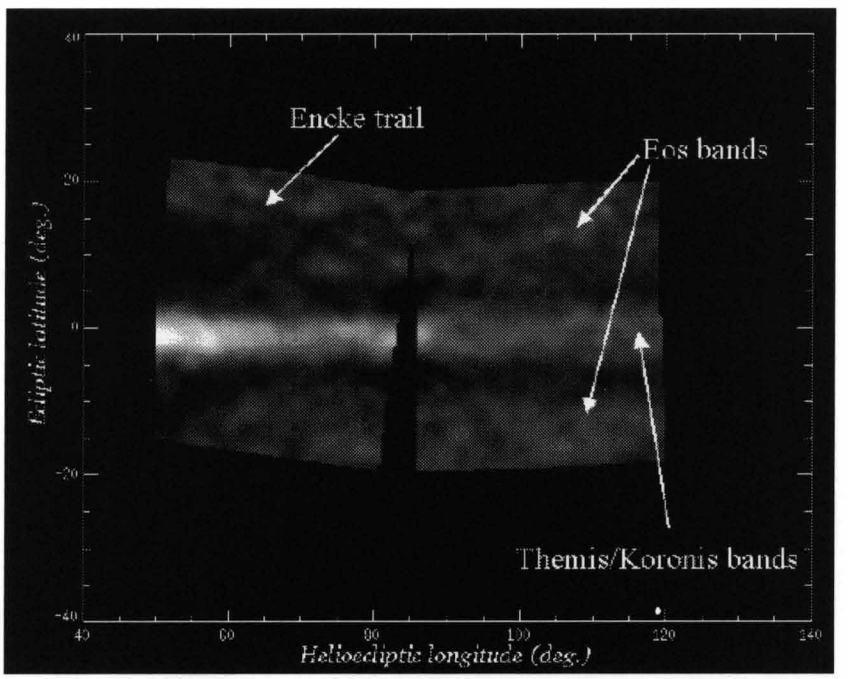

Figure 20: The result processed by using the Fourier filter to emphasize the structure of dust bands in the brightness distribution of the zodiacal light obtained by the ground-based observation on December 15, 1998. A bright spot at $\lambda - \lambda_{\odot} = 85°$ in the ecliptic plane is the scattered light from the Jupiter. The interplanetary dust bands associated with the asteroidal families of Themis, Koronis and Eos appear, as well as the cometary trail associated with comet P/Encke.

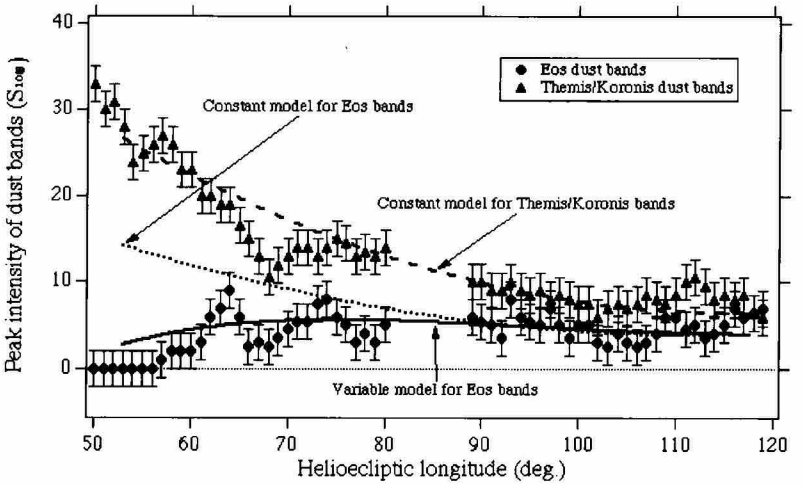

Figure 21: The peak intensities of the Themis/Koronis and the Eos dust bands as a function of a heliocentric longitude $\lambda - \lambda_\odot$. The observed results are shown as the filled triangles (Themis/Koronis) and the filled circles (Eos) with error bars (2 $S_{10\odot}$). The computed results of $(\lambda - \lambda_\odot)$-dependence of peak intensity are presented for the cases of two dust band models, i.e. a 'constant model' (a dashed curve for Themis/Koronis and a dotted curve for Eos) and a 'variable model' (a solid curve for Eos), which are defined in the text.

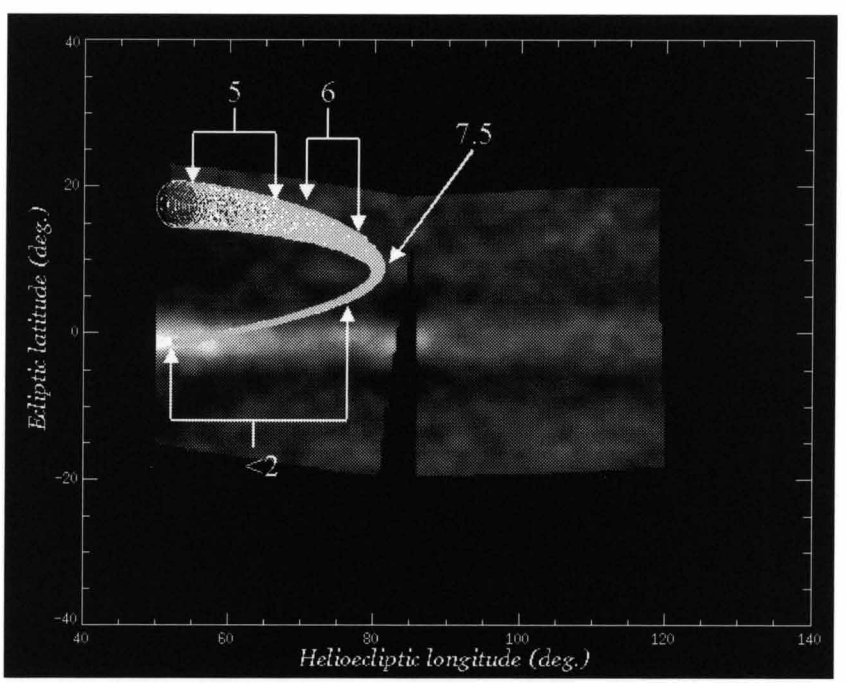

Figure 22: The dust trail associated with comet P/Encke. The dust tube with a radius of 0.015 AU along the orbit of comet P/Encke is illustrated. The numbers attached to the tube indicate the brightness in a unit of $S_{10\odot}$ calculated based on the dust tube model given in the text.

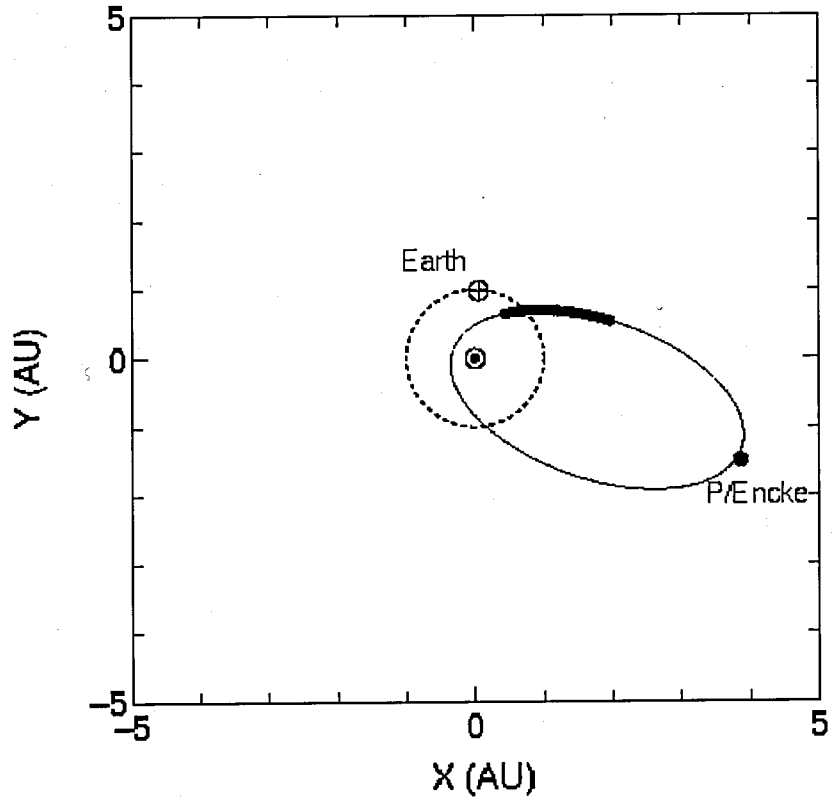

Figure 23: The location of the observed dust trail (thick curve) along the orbit of comet P/Encke projected on to the ecliptic plane on December 15, 1998.

Table I. Dispersion of inclination di (°) for each asteroidal family

	Themis family	Koronis family	Eos family
Large asteroid family[a]	0.166	0.042	0.270
Grogan et al. (1997)	~0.3	~0.1	2.5/3.5
Sykes (1990)	~0.2	~0.1	~1.4
Reach et al. (1997)	0.166	0.042	0.270
This work			
a constant model	0.3	0.1	1.0
a variable model for Eos bands			
(r≥2AU)			1.0
(r<2AU)			4.0

[a] cited in Reach et al.(1997).

6 General Conclusions

In this section, I summarize the results of this work.

In Chapter 2, we have reported the global structure of zodiacal light. It is found that (i)the locus of points of the maximum brightness of the morning zodiacal light is significantly shifted toward the south in September, while that of evening zodiacal light is shifted toward the north in March, (ii)the brightness distribution along the ecliptic latitude is asymmetry, (iii)the position of the maximum brightness of Gegenschein is deviated toward the south in September, in contrast with toward the north in February/March, (iv)the gradient of the relative intensity along a line perpendicular to the ecliptic is different with changing season. These trends can be explained by the zodiacal dust cloud model centered on the symmetric plane (if it exists) southward to the ecliptic plane in September and northward to in March, respectively.

In Chapter 3, we have presented the first ground-based observational evidence of the zodiacal dust bands originally discovered in the infrared wavelengths by the IRAS and confirmed by COBE. Photometric data of the morning zodiacal light have revealed the presence of zodiacal dust bands at ecliptic latitudes $\beta = 0°$, $3°$ and $\pm 10°$, as well as additional faint structures at approximately $\beta = \pm 5°$, between solar elongations $\epsilon = 75°$ and $90°$ ($270° \leq \lambda - \lambda_\odot \leq 285°$). Moreover, our observation of the Gegenschein has made a discovery of dust bands at β=$+2°, -4°$ and $-9°$ at $165° \leq \lambda - \lambda_\odot \leq 185°$. Using the separation of the inner dust band pair observed in two different regions of ϵ, we estimate the parallactic distance of this band pair to be about $1.6AU$ from the Sun.

In Chapter 4, we have examined the diversity and similarity of the visible dust bands and infrared dust bands, based on the data obtained by our ground-based observation (Ishiguro et al. 1999a) and by the Infrared Astronomical Satellite (IRAS). It is found that the latitude profile of visible dust bands at the solar elongation $\lambda - \lambda_\odot = 271°(\epsilon = 89°)$ is similar to that of infrared dust bands, except the appearance of the bands found at the ecliptic latitude $\beta = \pm 5°$ in the visible alone. Using the migration model for the spatial distribution of interplanetary dust bands(Reach et al.1997), originally deduced from the infrared data, we performed a prediction of the visible band structure near the anti-solar point to examine our observed evidence. Our results verify that the visible dust bands at $\beta = +2°$ and $-4°$ near the anti-solar point are composed of the dust particles originally supplied from the Themis and Koronis asteroid families.

Finally, in Chapter 5, we have shown our new findings, *i.e.* the evidence of dynamical evolution of dust bands particles, by using the photometric data of zodiacal light obtained at Mauna Kea, Hawaii ($4200m$) on December 15 1998. Namely, the new data have revealed that (1) the feature of the Eos dust bands detected at $\beta = \pm 10°$ becomes faint with decreasing the helioecliptic longitude, and finally fades out in $\lambda - \lambda_\odot \leq 60°$, while the brightness of the Themis/Koronis dust bands increases with decreasing the $\lambda - \lambda_\odot$. Our model calculations suggest that such an ϵ-dependence of band feature arises from the Eos band structure with increasing a dispersion in the orbital inclinations as the particles approach the Sun. Furthermore,(2) the dust trail associated with comet P/Encke has been detected in the visible for the first time. It is found that the visible dust trail is wider,

about $0.03AU$ in diameter, than the infrared dust trail. (3) In our previous observations performed in 1997 (Ishiguro et al. 1999a), we have found the dust bands at $\beta = \pm 5°$ without the definite parent body. It could be a partial or temporary dust band since we do not observe it in the present observation in 1998.

We have succeeded to detect the interplanetary dust bands. This is the first evidence from the ground-based visible observation. This exciting results were brought not only from the cooled CCD camera and best site of observation, but also from the careful examination of the sensitivities of detector in the laboratory and the state-of-the-art data reductions by using the original software which was developed in our laboratory. Our observations have opened the possibility of future advancing our knowledge of dust cloud in the solar system combining the in situ detections by satellites.

I am sure that our observation system of interplanetary dust features from the ground described here will provide further valuable information for the origin and evolution of the interplanetary dust cloud. These system developed in Kobe is opened for all researchers who are interested in the science topics being covered by potential observations. Please contact to the author when you need the help.

Acknowledgments

Many people have contributed to this study. First of all, I extremely thanks to Prof. Tadashi Mukai and Dr. Ryosuke Nakamura of Kobe University, Japan, for providing helpful comments and suggestion. I am also grateful to the Dr. J.F.James(Univ. of Manchester) and Hideo Fukushima(NAOJ), for giving me the technical advice on the CCD observation. In addition, appreciation is expressed to members of the SUBARU Project office(NAOJ), especially Dr. Kaz Sekiguchi, Kiso Observatory(Univ. of Tokyo) and Norikura Corona Observatory(NAOJ), who gave me their kind helps during the observations. I would like to thank Dr. Makoto Taguchi(NIPR) for his assistance with taking the flat frames at NIPR, and Prof. S.S.Hong(Seoul Univ.), Dr. Mark Sykes(Univ. of Arizona), William T.Reach(Caltech) for providing useful advice on this study. Finally, I thank my colleagues in Solar System Physics Group of Graduate School of Sci. & Tech. in Kobe University. In particular, this paper would not have been accomplished without cooperation with the member of zodiacal light observation team, especially Yasumasa Fujii and Chiaki Yoshishita.

References

Backman, D.E., L.J.Caroff, S.A.Sandford & D.H.Wooden, *Exozodiacal Dust Workshop ; Conference Proceedings*, NASA/CP, (1998).

CFHT Observers' Manual Version 5.0,
http://www.cfht.hawaii.edu/Instruments/ObserverManual/

Dermott, S.F., P.D.Nicholson, J.A.Burns & R.Houck, *Nature*, **312**, 505, (1984).

Dermott, S.F., R.S.Gomes, D.D.Durda, B.Å.S.Gustafson, S.Jayaraman, Y.L.Xu & P.D.Nicholson, *Chaos, Resonance and Collective Dynamical Phenomena in the Solar System ed. S.Ferraz-Mello (Kluwer, Dordrecht)*, 333, (1992).

Dermott, S.F., D.D.Durda, B.Å.S.Gustafson, S.Jayaraman, J.C.Liou & Y.L.Xu, *in Asteroids, Comets, Meteors ed A. Milani, M. Martini and A. Cellino (KLUWER ACADEMIC PUBLISHERS)*, 127, (1994a).

Dermott, S.F., S.Jayaraman, Y.L.Xu, B.Å.S.Gustafson & J.C.Liou, *Nature*, **369**, 719, (1994b).

Doressoundiram, A., M.A.Barucci, M.Fulchignoni & M.Florczak, *Icarus*, **131**, 15, (1998).

Dumont, R., *Ann. Astrophys.*, **28**, 265, (1965). (English Transl., NASA TT F11, **164**, 1965).

Dumont, R. & F.Sanchez-Martinez, *Ann. Astrophys.*, **31**, 293, (1968).

Grogan, K., S.F.Dermott, S.Jayaraman & Y.L.Xu, *Planet.Space Sci.* **45**, 1657, (1997).

Gustafson, B.Å.S., N.Y.Misconi & E.T.Rusk, *Icarus*, **72**, 568, (1987).

Grün, E., H.A.Zook, H.Fechtig, & R.H.Giese, *Icarus*, **62**, 244, (1985).

Hong, S.S., *A & A*, **146**, 67, (1985)

Hong, S.S. & S.M.Kwon, *Origin and Evolution of Interplanetary Dust, ed. by Levasseur-Regourd A.C. and Hasegawa H. (Kluwer Academic Publ.)*, 147, (1991).

Hong, S.S., S.M.Kwon, Y.-S.Park & C.Park, *Earth, Planets and Space*, **50**, 487, (1998).

IRAS Catalogs and Atlases: Explanatory Supplement 1988, ed. C.A. Beichman, G. Neugebauer, H.J. Habing, P.E. Clegg, T.J. Chester, (1988).

Ishiguro, M., R.Nakamura, T.Watanabe, T.Mukai, H.Tanabe, I.Mann, H.Kimura, P.Hillebrand & J.F.James, *Proc. of the 29th ISAS Lunar and Planetary Symp.*, **29**, 64, (1996).

Ishiguro, M., H.Nakayama, K.Ueda, H.Fukushima & T.Mukai, *Proc. of the 30th ISAS Lunar and Planetary Symp.*, **30**, 142, (1997).

Ishiguro, M., H.Fukushima, D.Kinoshita, T.Mukai, R.Nakamura, J.Watanabe & J.F.James, *Earth, Planets and Space*, **50**, 477, (1998).

Ishiguro, M., R.Nakamura, Y.Fujii, K.Morishige, H.Yano, H.Yasuda, S.Yokogawa & T.Mukai, *ApJ*, **511**, 432, (1999a, Paper I).

Ishiguro, M., R.Nakamura, Y.Fujii & T.Mukai, *PASJ*, **51**, 363, (1999b, Peper II).

Ishiguro, M., R.Nakamura, A.Nakata, Y.Fujii, S.Urakawa, C.Yoshishita & T.Mukai, (Submitted to *ApJ*).

Ishimoto, H., *Earth Planets Space*, **50**, 521, (1998).

James, J.F., T.Mukai, T.Watanabe, M.Ishiguro & R.Nakamura, *MNRAS*, **288 (No.4)**, 1022, (1997).

Leinert, C., *Space Sci. Rev*, **18**, 295, (1975).

Leinert, C., M.Hanner, I.Richter & I.Pitz, *A & A* **82**, 328-336, (1980).

Leinert, C., S.Bowyer, L.K.Haikala, M.S.Hanner, M.G.Hauser, A.-Ch.Levasseur-Regourd, I.Mann, K.Mattila, W.T.Reach, W.Schlosser, H.J.Staude, G.N.Toller, J.L.Weiland, J.L.Weinberg & A.N.Witt, *A&A Suppl.*, **127**, 1, (1998).

Low, F.J., D.A.Beintema, T.N.Gautier, F.C.Gillett, C.A.Beichman, G.Neugebauer, E.Young, H.H.Aumann, N.Boggess, J.P.Emerson, H.J.Habing, M.G.Hauser, J.R.Houck, M.Rowan-Robinson, B.T.Soifer, R.G.Walker & P.R.Wesselius, *ApJ*, **278**, L19, (1984).

Misconi, N.Y., *Icarus*, **47**, 265, (1981).

Mukai, T., *Highlights of Astronomy*, **8**, 305, (1989).

Mukai, T. & R.H.Giese, *A & A*, **131**, 355, (1984).

Roosen, R.G., *Icarus*, **13**, 523, (1970).

Roosen, R.G., *Rev. of Geophys. Space Phys.*, **9**, 275, (1971).

Reach, W.T., *ApJ*, **392**, 289, (1992).

Reach, W.T., B.A.Franz & J.L.Weiland, *Icarus*, **127**, 461, (1997).

Reach, W.T., M.V.Sykes, D.J.Lien & J.K.Davies, *DPS*, # 31, # 30-04R, (1999).

Spiesman, W.J., M.G.Hauser, T.Kelsall, C.M.Lisse, S.Harvey Moseley,Jr., W.T.Reach, R.F.Silverberg, S.W.Stemwedel & J.L.Weiland, *ApJ*, **442**, 662, (1995).

Staude, H.J., *A & A*, **39**, 325, (1975).

Sykes, M.V., *Science*, **232**, 1115, (1986).

Sykes, M.V., *ApJ*, **334**, L55, (1988)

Sykes, M.V., *Icarus*, **84**, 267, (1990).

Sykes, M.V., R.Greenberg, S.F.Dermott, P.D.Nicholson, J.A.Burns & T.N.Gautier, *in Asteroids II ed R.P.Binzel, T.Gehrels, M.S.Matthews (The Univ. of Arizona Press, Arizona)*, 336, (1989).

Sykes, M.V. & R.G.Walker, *Icarus*, **95**, 180, (1992).

Tanabe, H., *PASJ*, **17**, 339, (1965).

Van Rhijn, P.J., *ApJ*, **50**, 356, (1919).

Weinberg, J.L., M.S.Hanner, H.M.Mann, P.B.Hutchison & R.Fimmel, *Space Research*, **XIII**, 1187, (1973).